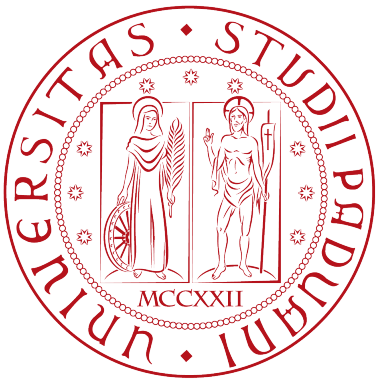

Università degli Studi di Padova

Dipartimento di Fisica e Astronomia "Galileo Galilei"

In collaborazione con:
KU Leuven - Departement Natuurkunde en Sterrenkunde

Corso di Laurea Magistrale in Fisica

Direct Observation of Strongly Confined Vortices in Superconductors

Relatore:
Prof. Giovanni Mattei
Correlatore:
Prof. Joris Van de Vondel

Laureando: Marco Perini
Matricola: 1080025

Anno Accademico 2014/2015

Contents

The story so far:
In the beginning the Universe was created.
This has made a lot of people very angry
and been widely regarded as a bad move.

Douglas Adams - The Hitchhiker's Guide to the Galaxy

Introduction

Superconductivity is one of the most fascinating phenomena in condensed matter physics, and after more than 100 years from its discovery, it is still far from being completely understood. The main feature of superconducting materials is their ability to carry electrical current without energy dissipation when cooled down under a certain critical temperature, which is different for every material [1]. But this astonishing property, which could be of key importance in future energy technology, comes at a price: the temperatures needed for superconductivity to set in are usually a few degrees above absolute zero, thus requiring powerful and energy-consuming cooling systems. The possibility to transport extremely high currents that can continue to flow for a potentially indefinite amount of time found a straightforward application in superconducting magnets, such as those used at the CERN laboratories [2] or the ones available for commercial Magnetic Resonance Imaging.
The other macroscopic phenomenon linked to superconductors is the so called Meissner effect, which can be described as the expulsion of magnetic field from inside a superconductor while cooled down to its critical temperature. In the so called type-I superconductors this effect lasts until the field reaches a critical value, at which superconductivity in the sample is totally destroyed. For type-II superconductors, the magnetic field penetrates inside the bulk in the form of vortices, that carry a quantized amount of magnetic field and where superconductivity is locally destroyed. In the presence of a current, these vortices are subjected to a Lorentz force, that causes them to move and to induce dissipation in the material.
What is currently limiting the use of superconductors for energy technologies is no more related to reaching extremely low temperatures, as the advent of high-T_c superconductors allowed tackling this issue with liquid-nitrogen cooling systems. The problem is the onset of dissipation due to magnetic vortices in type-II materials, as type-I present a critical magnetic field which is generally too low to allow a fruitful use of them for current transport. Controlling the behaviour of vortices is thus of fundamental importance for the development of truly dissipationless technology.

Secondly, superconductivity offers a wide range of possibilities for fundamental physics research: in these materials the charge carriers, the so-called Cooper pairs [3], organise themselves as to form a Bose-Einstein condensate. Several quantum phenomena can hence be investigated by studying the properties of superconductors, taking advantage of the macroscopic quantum coherence of the condensate.
When the size of the system is reduced as to reach the nanoscale, quantum effect as those related to confinement cannot be neglected. For example, shrinking the size of the super-

conducting condensate until its coherence length allows a tuning of the properties of the material, such as T_c and H_c. At the same time, confinement brings out phenomena that can be the basis for a new type of devices. Controlling the motion and pinning of single quantum fluxes, or fluxons, constitutes the basis of the emerging field of fluxonics, in the same way as electron charge and spin form the basis for electronic and spintronics respectively [4]. In addition to this, the property of flux quantization has played a key role in the development of superconducting flux qubits [5] for quantum computation technology. A more complete understanding of the behaviour of vortices in confined systems is thus of great interest for both fundamental and applied research perspectives.

The aim of this thesis work is to observe the effect of confinement on vortices in superconductors by means of Scanning Tunneling Microscopy (STM). It will be shown how this technique is extremely efficient in observing the vortex configuration, which is strongly influenced by the symmetry boundary conditions imposed by the geometrical shape of the nanostructures. Moreover, measurements regarding the energy barrier for vortex entrance in the nanostructures were performed, to understand its behaviour in the presence of defects and when an oscillating magnetic field is applied.
The outline of this thesis work is as follows:
In Chapter 1 the theoretical framework will be presented, starting with a general overview on superconductivity, as described by the theory of Ginzburg-Landau; in the second part of the chapter we will recall the main results of the theory of quantum tunneling.
Chapter 2 will provide a description of the experimental setup and of the different techniques used for fabrication, characterization and measurement of the samples.
The main results of the work and brief discussion will be presented in Chapter 3 and 4.

Chapter 1

Theoretical background

1.1 Superconductivity

1.1.1 General remarks

Superconductivity was discovered in 1911 by H. K. Onnes, who was studying the behaviour of the electric resistance of solid mercury at cryogenic temperatures. He observed that the resistance dropped abruptly to zero at a temperature of 4.2 K, and all attempts to find traces of resistance in the material were to no avail [6]. With modern equipment we can measure that the resistivity of superconductors is zero at the level of 10^{-24} Ω m. After mercury, several other materials were discovered to present a similar behaviour, among which tin, lead, niobium, aluminum and others.
The temperature at which the transition between normal and superconductor states happens is called critical temperature, T_c. However, superconductivity can be also be destroyed by applying a sufficiently strong magnetic field, called critical magnetic field, H_c. The temperature dependence of the critical field is well described by the empirical formula [1]:

$$H_c(T) = H_c(0)[1 - (T/T_c)^2] \tag{1.1}$$

where $H_c(0)$ is the critical field at T = 0 K.

In 1933 W. Meissner and R. Ochsenfeld discovered that, during the transition to the superconducting state, the magnetic field is expelled from a superconductor [7], regardless whether cooling under T_c (Zero Field Cooling, ZFC) or applying the magnetic field (Field Cooling, FC) was done first (see Fig. 1.1 right panel). This discover demonstrated for the first time that superconductors were not simply perfect conductors (i.e. materials with zero electrical resistance), where a Field Cooling and a Zero Field Cooling would produce two very different final states (see Figure 1.1 left panel). In fact, superconductors were found to be a whole new class of materials, with their own specific thermodynamical properties. This effect was explained theoretically in 1935 by F. and H. London, who provided the first phenomenological theory of superconductivity, based on a two-fluid approach. The theory predicted how the magnetic field, as well as induced supercurrents, could penetrate inside a superconductor following an exponential decay with characteristic lentgth scale λ, denoted as the London penetration depth.
However this theory, based on the laws of classical electrodynamics, failed at explaining

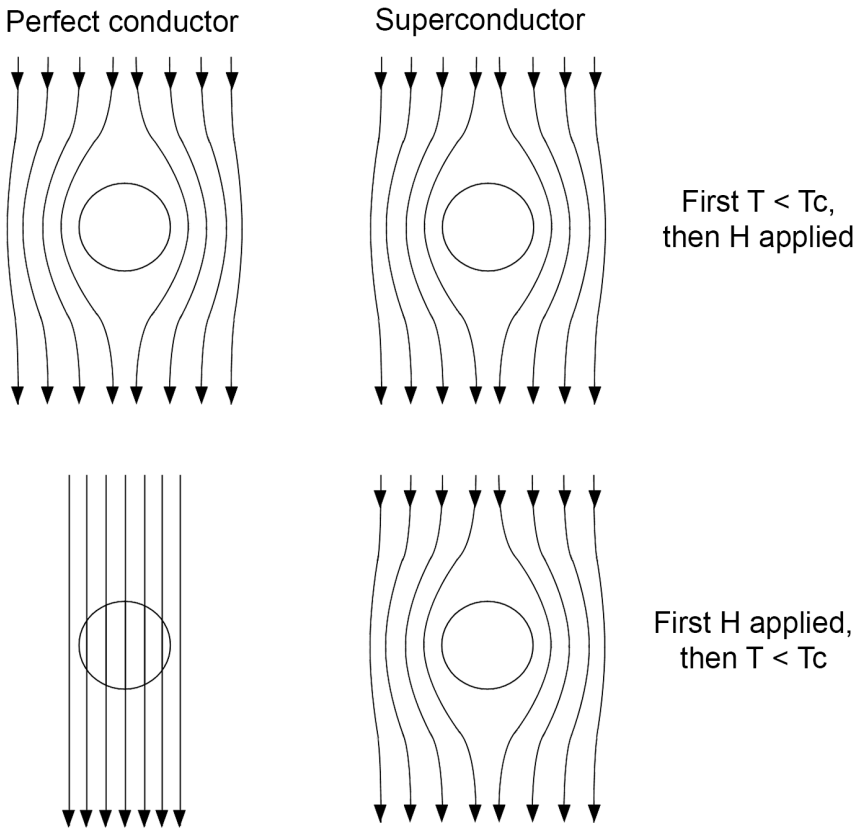

Figure 1.1: A perfect conductor and a superconductor exhibit the same behaviour when cooled under T_c before applying a magnetic field H, but if the two steps are switched the final state for the two materials is different.

several phenomena observed in superconductors (such as the behaviour of superconductors at the interface with a normal metal), and only in 1950 a phenomenological theory taking into account quantum effects was developed by V. L. Ginzburg and L. D. Landau [8].

1.1.2 Ginzburg-Landau Theory

A quantum theory of superconductivity needs firstly to take into account a complex wavefunction $\Psi(\mathbf{r}) = |\Psi(\mathbf{r})|\ e^{i\theta(\mathbf{r})}$ to describe the quantum behaviour of superconducting electrons, where $\theta(\mathbf{r})$ represents the phase of the wavefunction. Secondly, the transition between the normal and the superconducting states (in the zero magnetic field case) is regarded as a second-order phase transition, introducing an order parameter which is nonzero at $T < T_c$ and vanishes for $T = T_c$.
The stroke of genius that brought Ginzburg a Nobel Prize [9] was to combine these two aspects together, as the order parameter is chosen to be the effective wavenfuction $\Psi(\mathbf{r})$, whose square modulus represents the density of superconducting electrons n_s. Ψ was chosen to depend only on one spatial coordinate $\mathbf{r}$, as Landau and Ginzburg conjectured that superconducting electrons possessed bosonic properties and were all condensed on the ground

level of the system. This conjecture was found to be correct only with the advent of the Bardeen-Cooper-Schrieffer (BCS) theory in 1957 [10], that explained how pairs of electrons interact via the phonons of the material as to form integer-spin particles called Cooper pairs, which are the charge carriers in superconductors.

The starting point of the Ginzburg-Landau (GL) theory is the theory of second-order phase transition developed by Landau [11]: according to that, a phase transition is of second order when the state of the system, and the order parameter, changes gradually while its symmetry undergoes a discontinuous change at the transition temperature, specifically from a high-temperature and low-ordered phase (where the order parameter is zero) to a low-temperature and higher-ordered phase (where the order parameter is nonzero). Being a phase-transition theory, the GL theory is valid only in a neighbourhood of the critical temperature, $T_c - T \ll T_c$.

The Landau theory is based on the assumption that the free energy of a system close to the transition point can be expanded in powers of the order parameter, as the latter is small when approaching the phase transition. For a homogeneous superconductor in the absence of a magnetic field, the expansion can be carried out as follows:

$$F_{s0} = F_n + \alpha|\Psi|^2 + \frac{\beta}{2}|\Psi|^4 + o(|\Psi|^6) \tag{1.2}$$

where F_{s0} is the free energy density of the superconductor, F_n is the free energy in the normal state, α and β some material-dependent expansion coefficients, and

$$|\Psi|^2 = |\Psi(\mathbf{r})|^2 = n_s/2 \tag{1.3}$$

is the density of superconducting electrons, divided by 2 because we know that these superconducting electrons are actually pairs. The free energy does not contain odd-terms in $|\Psi|$ because the meaningful physical quantity is $|\Psi|^2$, the density of particles. A simple calculation shows that the free energy minimum in this case is given by:

$$|\Psi|^2 \doteq |\Psi_0|^2 = -\alpha/\beta. \tag{1.4}$$

It's possible to define a dimensionless wavefunction

$$\psi(\mathbf{r}) = \Psi(\mathbf{r})/\Psi_0$$

that is normalized to the density of superconducting electrons Ψ_0 for a homogeneous superconductor. Hence ψ takes values between 0 (completely normal state) and 1 (completely superconducting state) and gives account for the "strength" of the superconducting behaviour.

For the more general case of an inhomogeneous superconductor in a uniform magnetic field, the Gibbs free energy is:

$$G_{sH} = F_{sH} - \frac{\mathbf{H}\cdot\mathbf{H_0}}{4\pi} = G_n + \alpha|\Psi|^2 + \frac{\beta}{2}|\Psi|^4 + \frac{H^2}{8\pi} + \frac{1}{2m}\left|-i\hbar\nabla\Psi - \frac{2e}{c}\mathbf{A}\Psi\right|^2 - \frac{\mathbf{H}\cdot\mathbf{H_0}}{4\pi}. \tag{1.5}$$

where G_n is the normal state energy, $\mathbf{H}_0$ is the external magnetic field and $\mathbf{H}$ is the local microscopic field at a given point of the superconductor. The fourth term stands for the magnetic energy density, and the fifth one is the kinetic energy density of the superconducting electrons. In basic quantum mechanics the kinetic energy density is linked to the operator $-i\hbar\nabla$, which has to be modified in the presence of a magnetic field:

$$-i\hbar\nabla \rightarrow -i\hbar\nabla - \frac{e}{c}\mathbf{A} = m\mathbf{v}$$

so that the velocity operator takes the form:

$$\mathbf{v} = \frac{1}{m}\left(-i\hbar\nabla - \frac{e}{c}\mathbf{A}\right). \tag{1.6}$$

In Eq. 1.5 m is the mass of the Cooper pair, and similarly the charge e has been replaced with $2e$ for the same reason.

The next step is now to integrate the Gibbs free energy over the volume of the superconductor, and then minimize it with respect to Ψ and $\mathbf{A}$. We then obtain the two GL equations, firstly the one for the order parameter:

$$\alpha\Psi + \beta\Psi|\Psi|^2 + \frac{1}{4m}\left(i\hbar\nabla + \frac{2e}{c}\mathbf{A}\right)^2\Psi = 0 \tag{1.7}$$

with boundary conditions depending on the specific problem. For a superconductor in contact with vacuum, where no current should pass through the superconductor-vacuum interface, this becomes:

$$\left(i\hbar\nabla\Psi + \frac{2e}{c}\mathbf{A}\Psi\right)\cdot\mathbf{n} = 0 \tag{1.8}$$

where $\mathbf{n}$ is the unit vector perpendicular to the superconductor surface. The second GL equation, the one for the vector potential, is:

$$\mathbf{j_s} = \frac{c}{4\pi}\nabla\times\nabla\times\mathbf{A} = -i\frac{\hbar e}{2m}(\Psi^*\nabla\Psi - \Psi\nabla\Psi^*) - \frac{2e^2}{mc}|\Psi|^2\mathbf{A} \tag{1.9}$$

with $\mathbf{j}_s$ the supercurrent density. A more elegant form for these equations is obtained introducing two characteristic lengths:

$$\xi^2 = \frac{\hbar^2}{4m|\alpha|}, \qquad \lambda^2 = \frac{mc^2\beta}{8\pi e^2\alpha} \tag{1.10}$$

and using the normalized order parameter ψ.

The GL equations can be hence re-written as follows:

$$-\psi + \psi|\psi|^2 + \xi^2\left(i\nabla + \frac{2\pi}{\Phi_0}\mathbf{A}\right)^2\psi = 0 \tag{1.11}$$

$$\mathbf{j_s} = \frac{2c\ \Phi_0}{(4\pi\lambda)^2}\ |\psi|^2\left(\nabla\theta(\mathbf{r}) - \frac{2\pi}{\Phi_0}\mathbf{A}\right) \tag{1.12}$$

where in the last equation we recall that $\psi = |\psi|^2 e^{i\theta(\mathbf{r})}$, and $\Phi_0 = \pi\hbar c/e$ is denoted as quantum of magnetic flux.
It can be noticed that Eq. 1.11 resembles the time-independent Schrödinger equation with a non-linear term $\psi|\psi|^2$.
These two coupled differential equations can be self-consistently solved in order to obtain the spatial distribution of the order parameter $\psi(\mathbf{r})$ and the current density $\mathbf{j_s}(\mathbf{r})$ inside the superconductor, and thus they provide the starting point for every calculation based on the GL theory.

In Eq 1.10 we introduced two lengthscales, ξ and λ, which are of fundamental relevance to understand the behaviour of the superconducting condensate. λ is the magnetic penetration depth, whose role is clear when looking at the decay of magnetic field inside a superconductor:

$$H(x) = H_0 \; e^{-x/\lambda}. \tag{1.13}$$

where H_0 is the magnetic field at the surface of the superconductor.
The second characteristic length, ξ, is denoted as coherence length, and stands for the typical lengthscale over which the order parameter can change significantly, for example when in contact with a normal metal.
Both ξ and λ are material dependent, as they are strongly correlated to the electron mean free path l and to the average distance between two electrons in a Cooper pair, ξ_0. In the so-called dirty limit, when $l \ll \xi_0$, their temperature dependence is [12]:

$$\xi(T) = 0.855\sqrt{\frac{\xi_0 \; l}{1 - \frac{T}{T_c}}} \tag{1.14}$$

$$\lambda(T) = 0.64 \; \lambda_L(0)\sqrt{\frac{\xi_0}{l}\frac{1}{1 - \frac{T}{T_c}}}. \tag{1.15}$$

where $\lambda_L(0)$ is the London penetration depth at zero temperature. Both lengths diverge for $\mathrm{T} \to \mathrm{T}_c$. The dirty limit is chosen as it is the correct approximation for the nanostructures considered in this work.
We can also define the temperature independent Ginzburg-Landau parameter:

$$k = \frac{\lambda(T)}{\xi(T)} \tag{1.16}$$

whose role will be outlined in greater detail in Sec. 1.1.4.

1.1.3 Magnetic Flux Quantization

An interesting property emerges from the requirement of ψ being single-valued in every point in space. As a consequence, the phase $\theta(\mathbf{r})$, when making any closed path inside a superconductor, has to return to itself plus an integer (including zero) multiple of 2π. If we consider a superconductor with a hole in it, we can take a closed path C including the hole and far enough from its surface, so that $\mathbf{j_s} = 0$ all along the contour.

From Eq. 1.12 it follows that:

$$0 = \oint_C \mathbf{j_s} \cdot dl = \oint_C \nabla\theta(\mathbf{r}) \cdot dl - \frac{2\pi}{\Phi_0} \oint_C \mathbf{A} \cdot dl \tag{1.17}$$

and using Stoke's theorem:

$$\oint_C \mathbf{A} \cdot dl = \int\int_{S(C)} \nabla \times \mathbf{A} \cdot d\Sigma = \Phi \tag{1.18}$$

where $S(C)$ is the surface with border C and Φ is the magnetic flux through $S(C)$.
Hence Φ is related to the total variation of the phase of the wavefunction over a closed contour, which is now known to be $2\pi n$, where n is an integer number. Thus we obtain:

$$\Phi = \frac{\Phi_0}{2\pi} \oint_C \nabla\theta(\mathbf{r}) \cdot dl = n\Phi_0 \tag{1.19}$$

meaning that the magnetic flux inside the hole can only assume discrete values, which are multiples of $\Phi_0 = hc/2e = 2.07 \times 10^{-7}$ G cm^2.
The physical origin of the flux quantization is the same as the quantization of the orbits of electrons in atoms, which is that the electronic wavefunction must contain an integer number of wavelengths over the closed orbit. However, a remarkable difference with this example is that flux quantization takes place on a macroscopic rather than atomic scale, thus being a clear example of a macroscopic quantum effect, as if we were working on a "macroscopic" atom. This effect will be of key importance to study vortex behaviour in superconductors.

1.1.4 Type-I and Type-II superconductivity

In Eq. 1.16 we introduced a dimensionless parameter k, which defines the relation between the magnetic penetration depth and the coherence length. This relation is necessary to study how the energy of the system is modified when a magnetic field tries to penetrate inside a superconductor. As an example, let's consider a superconductor in the $x > 0$ half-plane in contact with a normal metal in the $x < 0$ one.

From simple energy considerations it is easy to show that the Gibbs free energy density far from the interface is the same for the two regions. We can then define a surface energy σ_{ns} as:

$$\sigma_{ns} = \int_{-\infty}^{+\infty} (G_{sH} - G_n) dx \tag{1.20}$$

where G_{sH} is the Gibbs energy density at the interface, defined in Eq. 1.5, and G_n is the free energy density far into the normal region, given by:

$$G_n = F_n - \mathbf{H} \cdot \mathbf{H_0}/8\pi = F_n - H_0^2/8\pi. \tag{1.21}$$

In the two limiting cases the surface energy is positive ($\lambda \ll \xi$) and negative ($\lambda \gg \xi$), giving rise to a different response to an applied magnetic field.

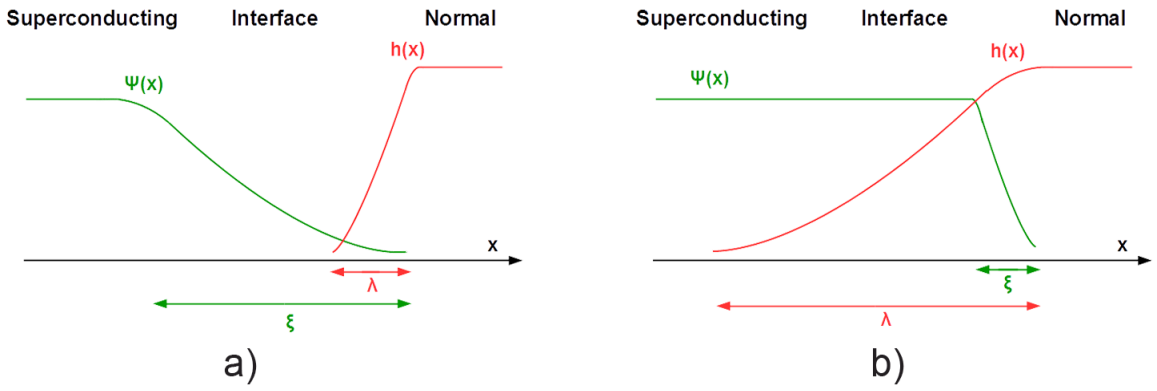

Figure 1.2: Spatial variation of the order parameter and of the magnetic field at the interface between a normal metal and a superconductor when $\lambda \ll \xi$ (**a**) and $\lambda \gg \xi$ (**b**).

When $\lambda \ll \xi$, at the interface there is a region of thickness ξ where the order parameter is nonzero and there is no magnetic field (see Fig. 1.2a). As Cooper pairs condense at a smaller energy value than the electron ground state, a region where ψ is lower than 1 has an additional energy compared to where $\psi = 1$. Thus in this case $\sigma_{ns} > 0$, which means that it's energetically favourable for the system to expel the magnetic field from the inside of the superconductor (the so-called Meissner state) and to minimize the total area of the interface with the normal metal.

When $\lambda \gg \xi$, in a region of thickness λ the order parameter is 1 and there is a non-negligible magnetic field (see Fig. 1.2b). Compared to a normal region with the same magnetic field, the interface region has a smaller energy, as its electrons have condensed into Cooper pairs, and in this case $\sigma_{ns} < 0$. This means that the system will try to minimize

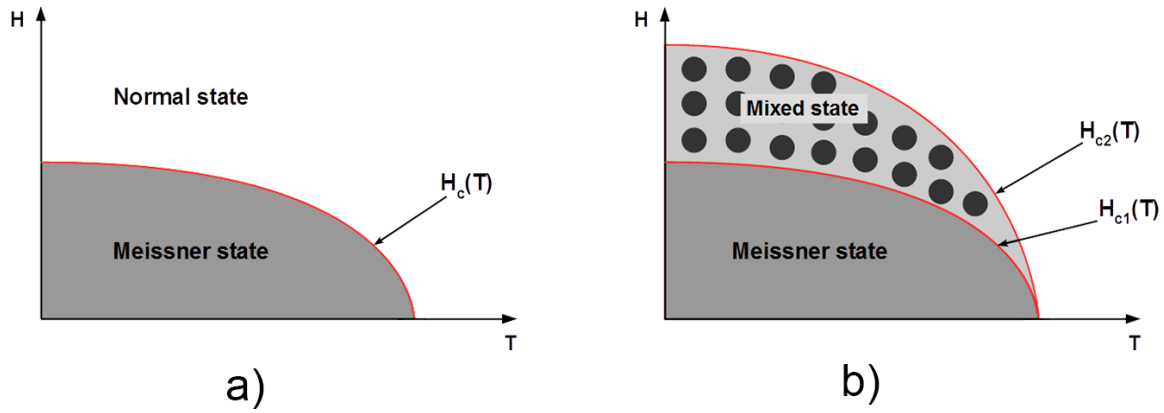

Figure 1.3: Phase diagram H(T) for a type-I (**a**) and type-II (**b**) superconductor. In the latter case the Meissner state is present below $H_{c1}(T)$, while above it, in the mized state, the field penetrates as vortices.

its energy by creating interfaces between superconducting and normal state. Combining this with the fluxoid quantization requirement, it results that the superconductor will allow the penetration of an external magnetic field as quantized units of flux, or vortices, maximizing the amount of interfaces with the normal state.

Those superconductors for which $\sigma_{ns} > 0$ are called type-I superconductors, while those having $\sigma_{ns} < 0$ are type-II superconductors. In the first case the Meissner state is visible until the applied field reaches a critical value and superconductivity is destroyed (see Fig. 1.3a). In type-II materials the Meissner state is still visible below the so called first critical field H_{c1}, after which the vortex state, or mixed state, sets in (see Fig. 1.3b). Increasing the magnetic field gets vortices closer and closer, until the normal cores overlap and the normal state is reached at the second critical field H_{c2}. Exact calculations show that materials with $k < 1/\sqrt{2}$ exhibit a type-I behaviour, while those with $k > 1/\sqrt{2}$ are type-II.
While most of the elemental superconductors are type-I, metal alloys and more complex compounds show type-II behaviour. All high temperature superconductors are type-II, as well as boron-doped diamond and silicon.

1.1.5 Vortex structure and arrangement

As already mentioned before, in type-II superconductors the magnetic field can penetrate inside the material forming cylindrical filaments that carry a quantized amount of magnetic flux. Supercurrents circle around these filaments to keep the magnetic field value, with

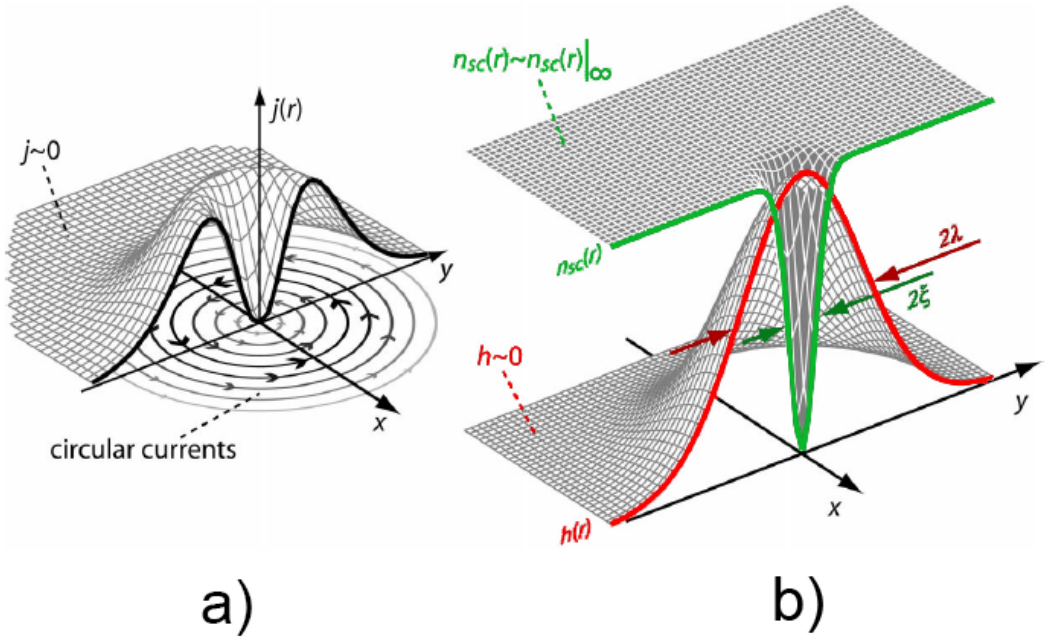

Figure 1.4: **a**: Current distribution around the normal core of a vortex. **b**: Density of Cooper pairs $n_{sc}(r)(\sim \psi)$ and local magnetic field $h(r)$ in and around a vortex. Taken from [4]

increasing velocity while going towards the center of the filament. To avoid a velocity divergence, superconductivity in the central region is gradually destroyed, thus leaving a normal core that slowly recovers its superconducting features moving radially from the center. Each filament, or vortex, is then composed of a normal core, with size $\sim 2\xi$, where $\psi \sim 0$, around which supercurrents flow decreasing exponentially in intensity over a length λ in the radial direction. The magnetic field follows a similar decay, and the whole structure of the vortex is shown in Fig. 1.4.

As the magnetic field is increased further above H_{c1}, more vortices will be present inside the superconductor and when their distance becomes comparable to λ it is no longer possible to consider them as single non-interacting unities. A qualitative description of the interaction between two vortices can be made using fluidodynamical considerations. If two vortices come close, in the region between them the net circulating current will be lower, as the respective currents are flowing in opposite directions there. This means that in this region the Bernoulli pressure is higher, thus producing a repulsive force, as shown in Fig. 1.5a. More generally, it is possible to show that in an arbitrary array of vortices the force per unit of length acting on a single flux line is given by:

$$\mathbf{f_L} = \frac{1}{c} \left[\mathbf{j_s} \times \phi_\mathbf{0} \right] \tag{1.22}$$

where $\mathbf{j_s}$ is the total supercurrent density at the center of the vortex core, and $\phi_\mathbf{0}$ is its magnetic flux. It is then evident that vortices with same polarity will repel each other, and the whole system will arrange itself in the lowest energy configuration. This is shown to be a triangular vortex lattice (see Fig. 1.5b), also known as Abrikosov lattice in honour of A. A. Abrikosov, who first proposed a detailed theory of type-II superconductors [13].

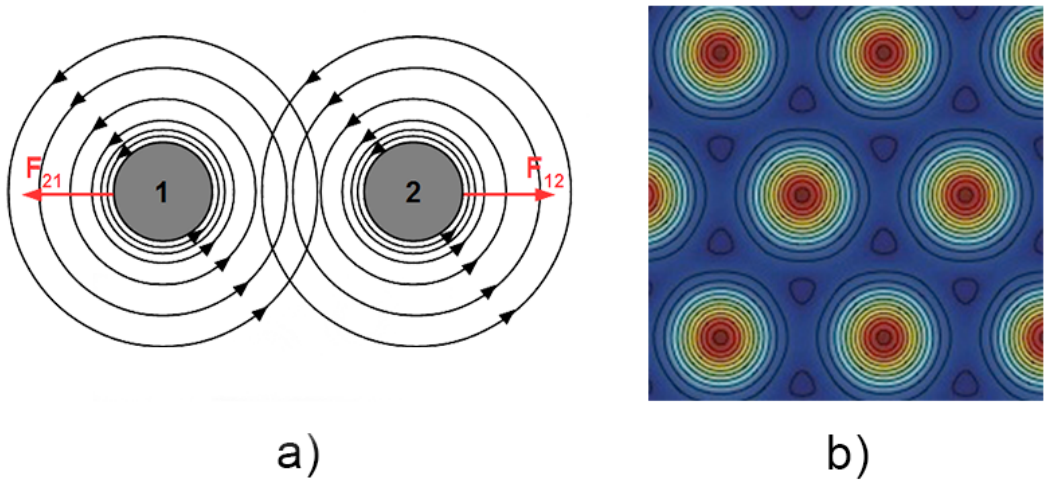

Figure 1.5: a: Schematic of mutual vortex repulsion. **b:** The Abrikosov lattice

The first direct observation of the Abrikosov lattice is due to Trauble and Essmann [14], who used ferromagnetic nanoparticles on top of a type-II superconducting surface to detect

where the magnetic field lines emerged from the superconductor. Successively, many other direct observations were performed with different techniques [15] [16] [17].

Eq. 1.22 also shows that as soon as a supercurrent is applied to a perfectly homogeneous type-II superconductor, vortices will start to move inside the material, leading to energy dissipation [18]. However, many kinds of defects in the materials act as pinning centers, meaning that they exert an attractive force on vortices that keeps them from moving. The role of these pinning centers is then extremely important in order to obtain truly dissipationless current transport.

1.1.6 Going to the Mesoscopic Scale

Interesting effects can arise when the size of the system becomes comparable with λ or ξ, as confinement effects due to the edge of the sample and to screening currents start acquiring a relevant role. This can be understood with a simple example: let's consider a slab of superconducting material which is in contact with vacuum on two of its sides (see Fig. 1.6c). The first GL equation can be used to determine the variation of the order parameter inside the superconductor. Interestingly, if we neglect the nonlinear term $\psi|\psi|^2$ in Eq. 1.11, we obtain:

$$\left(i\nabla + \frac{2\pi}{\Phi_0}\mathbf{A}\right)^2 \psi = \frac{4m|\alpha|}{\hbar^2}\psi \tag{1.23}$$

which is the analogue of a Schrödinger equation for the order parameter, with energy eigenvalues $4m|\alpha|/\hbar^2$. Using the same boundary condition as in Eq. 1.8 for a superconductor-vacuum interface, we are now dealing with the usual "particle in a box" problem, where confinement effects are visible on the eigenvalues spectrum when reducing the size of the box.
Confining the superconducting condensate can for example give rise to vortex configurations which are significantly different from the usual Abrikosov lattice, and it is also possible to define states with different vorticity L, i.e. states with a fixed number of vortices. This difference with macroscopic samples is shown in Fig. 1.6a, b and d, where the magnetization curves for macroscopic type-I, type-II and mesoscopic type-II superconductors are compared. In a macroscopic type-II sample vortices appear as an organised lattice once H_{c1} is reached, and the whole state is destroyed when reaching H_{c2}, when the inter-vortex distance is so small that they start to overlap. In a mesoscopic system the magnetization presents a series of sudden drops, each corresponding to the entrance of a quantum of magnetic flux inside the superconductor.

What is interesting to study is how vortices arrange in these L-fixed states. Numerous theoretical (e.g. [20] and [21]) and experimental ([17], [21] among the others) works have investigated vortex behaviour in the so called weak confinement regime, when the system size is comparable to the penetration depth λ. What has emerged is that the geometrical shape of the confining nanostructures, which impose specific boundary conditions to the condensate, is the main factor influencing the vortex configuration.

Theoretical studies were also performed to study the strong confinement regime, i.e.

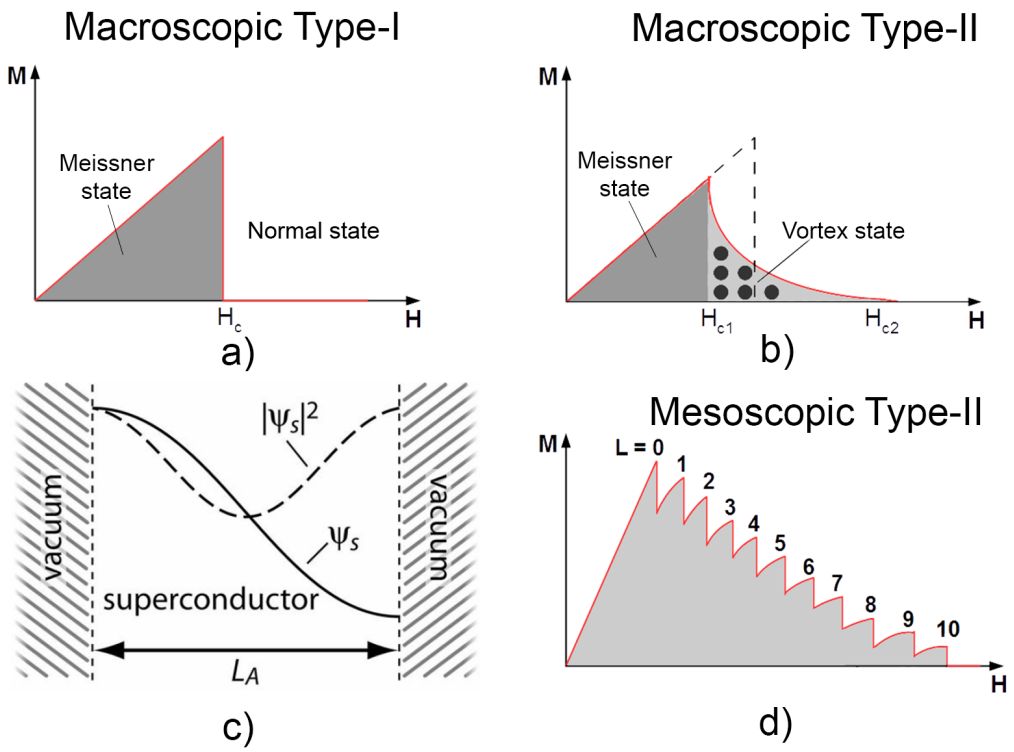

Figure 1.6: a, b, d: Magnetization curves as a function of the applied magnetic field. In a type-I superconductor the Meissner state (S) exists until the critical field is reached, then the normal state sets in. In a macroscopic type-II, the Meissner state exists until the value H_{c1}, above which the vortex state is observed until H_{c2}. In a mesoscopic type-II states with different vorticity L are clearly visible, and there is no vortex lattice anymore. **c**: Schematics of superconducting condensate confinement. ψ_s stands for the order parameter.

when the system has comparable dimensions with ξ, which is much smaller than λ in type-II materials. As already stated before, screening currents at the surface usually decay in intensity towards the interior of the material with decay length λ. If the whole system is smaller than λ, this implies that those currents never vanish completely inside the superconductor, and their interplay with vortices is not negligible anymore. Because of this, symmetry-induced configurations [19] [22] and several exotic states are predicted to arise in this regime, such as giant vortex [23] and vortex-antivortex states [24].
Few experimental works have been carried out regarding strongly confined vortices in superconductors. Transport measurements were used to study the H-T phase boundary in mesoscopic samples [25], but to directly observe the vortex behaviour scanning probe methods are more suitable. Magnetic techniques such as Bitter decoration, scanning SQUID microscopy and scanning Hall microscopy are of no use for this purpose, as they record differences of the order of λ, which can be much larger than the size of the system.
Scanning Tunneling Microscopy probes the local density of states of the sample, which varies in a lengthscale of the order of ξ, and is thus an extremely powerful tool for the investigation of vortex matter in very strong confinement regimes. This was shown in recent

studies of STM on as-grown Pb islands, that brought to the experimental observation of giant vortex states [26] and Josephson vortices [27]. However, because of the growth method, those Pb islands do not present a defined shape, and cannot thus be used to confirm theoretical predictions on symmetrical structures. No experimental work has been carried out so far regarding an STM study of symmetrical superconducting nanostructures. Our work is thus a first of its kind STM analysis of strongly confined vortices in superconductors.

The key instrument to perform this analysis is then the Scanning Tunneling Microscope. For this reason, the next section will resume the basics of the theory on which STM relies, which is quantum tunneling.

1.2 Tunneling Theory

Quantum tunneling refers to the phenomenon where a particle travels through a potential barrier which it could not classically overcome. This astonishing effect is made possible because of the wave-particle duality postulated by de Broglie [28]. A wave impinging upon a potential energy barrier does not go abruptly to zero inside of it, but rather decays exponentially in the inside. If the barrier is thin enough, the wave can appear at the other end of it. In the same way quantum particles can be described by means of wavefunctions, that decay as well exponentially inside a potential barrier if the energy of the particle is lower than the barrier. The tunnel effect is the non-zero probability of measuring the particle at the other side of the potential wall, and the particle is said to have tunneled through it.
The first to take notice of this effect was F. Hund [29] in 1927, while its first application was a mathematical explanation of the α decay by Gamow [30] and separately by Gurney and Condon [31]. In 1957 tunneling was then discovered to play a role in solid state physics, for the development of transistors and diodes, and in 1973 the Nobel prize was awarded to Josephson, Esaki and Giaever for their predictions regarding tunneling of electrons and Cooper pairs in semiconductors and superconductors [33].

1.2.1 Bardeen's approach to Quantum Tunneling

A simple treatment of tunneling can start considering a simple rectangular finite potential barrier, like the one shown in Fig. 1.7. If the transmission T through the barrier is small, a perturbative approach can be used. But instead of finding exact solutions for an approximate Hamiltonian, Bardeen [34] proposed an approximated solution to the exact Hamiltonian. The total Hamiltonian of the system can be written as:

$$H = H_0 + H_T = H_l + H_r + H_T \tag{1.24}$$

where $H_{l,r}$ account for the state of the system at the left and at the right of the barrier respectively, and H_T is the transfer Hamiltonian that describes tunneling of electrons from one side to the other. An approximate set of solutions is:

$$\begin{cases} \Psi_l(z) = ae^{-\chi z} & z \geq 0; \\ \Psi_r(z) = be^{\chi z} & z \leq s; \end{cases} \tag{1.25}$$

with $\chi = \sqrt{2m(V_0 - E)}/\hbar^2$. This means that the impinging wave from the left exponentially decays inside the barrier, and so does the transmitted wave on the right. In this way we have an analytical form for every z for Ψ_l and Ψ_r.

With them it is in principle possible to define an effective tunneling matrix element M_{rl}:

$$M_{rl} = \langle \Psi_r | \, H_T \, | \Psi_l \rangle = \int_{\infty}^{+\infty} \Psi_r^* \; H_T \; \Psi_l \; dz. \tag{1.26}$$

But while the two wavefunctions are known, there is no obvious way to define H_T. What Bardeen showed is that is possible to write the tunneling matrix element as:

$$M_{rl} = \frac{\hbar^2}{2m} \int_{S_{lr}} (\Psi_l \nabla \Psi_r^* - \Psi_r^* \nabla \Psi_l) \; dS \tag{1.27}$$

where S_{lr} is any surface lying in the potential barrier [35]. In this way the matrix element can be computed just knowing the wavefunctions outside the barrier. As we consider the tunneling as a perturbation, it is then possible to calculate the transmission rate for an electron in state l using the Fermi's Golden Rule [36]:

$$\Gamma_{rl} = \frac{2\pi}{\hbar} \; |M_{rl}|^2 \; \frac{dN_r}{dE} \tag{1.28}$$

where dN_r/dE is the density of final states r. In a 1D case like the one shown in Fig. 1.7 M_{rl} can be easily calculated considering Eq. 1.25:

$$M_{rl} \sim \frac{\hbar^2}{2m} \left(a e^{-\chi z} \frac{d}{dz}(b\chi e^{-\chi z}) - b e^{-\chi z} \frac{d}{dz}(a e^{-\chi z}) \right) = \frac{\hbar^2}{m} \; ab \; \chi \; e^{-2\chi z} \tag{1.29}$$

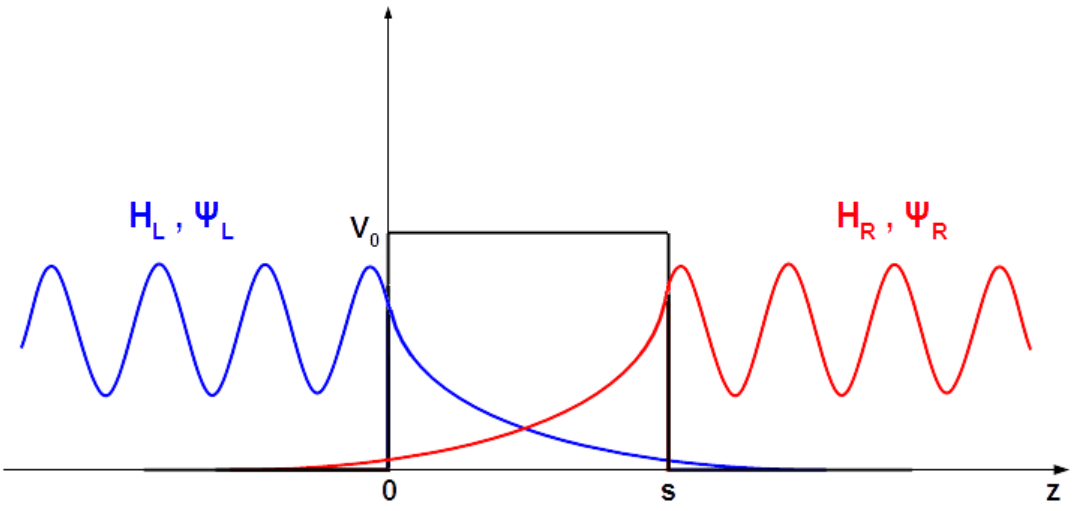

Figure 1.7: Schematics of a rectangular potential barrier and of the wavefunctions at the left (blue) and at the right (red) of it, in the Bardeen's approximation.

and consequently:

$$T \sim |M_{rl}|^2 \sim e^{-4\chi z}. \tag{1.30}$$

It's hence evident that tunneling between two electrodes depends significantly on their mutual distance, and this is the key point for the extremely high sensitivity of STM, as will be shown in Chapter 2.

After this brief overview of the main aspects of general tunneling theory, the specific case of tunneling between metallic electrodes will be now presented.

1.2.2 Giaever Tunneling

In 1960 I. Giaever performed a series of experiments to demonstrate tunneling of electrons between two metals, in the normal or superconducting state, separated by a thin oxide layer [37]. From these experiments he was able to demonstrate the existence of the superconducting energy gap, one of the most important prediction of the BCS theory of superconductivity, developed a few years before.

Let's first consider the case of tunneling between two metals, and let's limit the discussion to the case of elastic tunneling. We can assume the Fermi levels of the two metals, which are almost in contact, to be equal (see Fig. 1.8a). An estimate for the probability of electron tunneling from a certain state l of the left metal into a state r in the right metal can be obtained from Eq. 1.28:

$$\Gamma_{rl} = \frac{2\pi}{\hbar} \, |M_{rl}|^2 \, n_r \, (1 - f_r) \tag{1.31}$$

where n_r is the density of states on the right side and $(1 - f_r)$ is the probability of the state r being empty, as f_r is the Fermi-Dirac distribution.
Clearly, if the Fermi levels are equal, there are no free states r where the electrons in l can tunnel, and thus the net tunneling current is zero. By applying a bias voltage V between the two metals, the Fermi levels are shifted, so that empty states for tunneling appear. If we sum over the occupied states on the left, we can compute the total tunneling current of electrons from left to right:

$$j_{rl} \propto \int_{-\infty}^{+\infty} |M_{rl}|^2 \, n_l(E) \, n_r(E + eV) \, f_l(E) \, [1 - f_r(E + eV)] \, dE \tag{1.32}$$

where the density of occupied states $n_l(E)$ is weigthed with $f_l(E)$, the probability that the states are occupied. With a similar expression for j_{lr} it's possible to obtain the net tunneling current between the two metals:

$$j = j_{rl} - j_{lr} \propto \int_{-\infty}^{+\infty} |M|^2 \, n_l(E) \, n_r(E + eV) \, [f_l(E) - f_r(E + eV)] \, dE \tag{1.33}$$

where $|M| = |M_l| = |M_r|$. In the limit of small applied voltage and of zero temperature we therefore obtain:

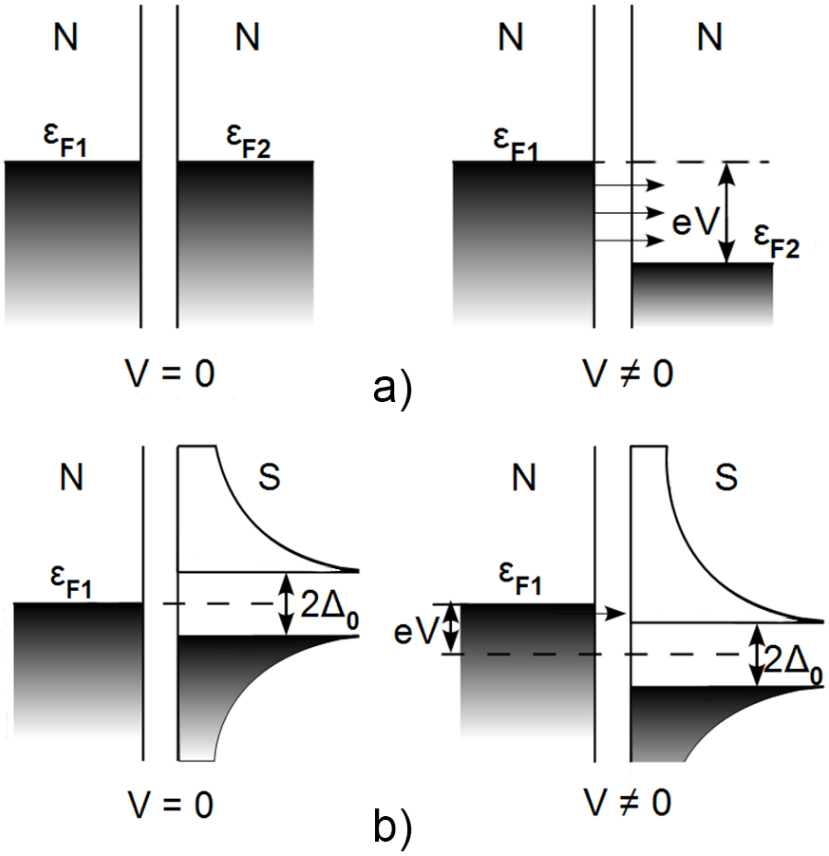

Figure 1.8: **a**: Tunnel junction at T=0 between two normal metals. **b**: Tunnel junction at T=0 between a normal and a superconducting metal.

$$j_{\mathbf{NN}} \propto n_l(E_F)\ n_r(E_F)\ eV \tag{1.34}$$

which means that the tunneling current between two metals is linearly proportional to the applied bias voltage.

The behaviour of the tunneling current changes significantly if one of the two metals is in the superconducting state. As predicted by the BCS theory, the density of states for a superconductor is:

$$n_s(E) = \begin{cases} n_N(0) \cdot \frac{|E|}{\sqrt{E^2-\Delta^2}} & |E| \geq \Delta \\ 0 & |E| < \Delta \end{cases} \tag{1.35}$$

with $n_N(0)$ the density of states of a normal metal at the Fermi energy, and E measured from the Fermi energy (see Fig. 1.8b). The net tunneling current between a normal and a superconducting metal is thus given by:

$$j_{\mathbf{SN}} \propto n_l(E_F)\, n_r(E_F) \int_{-\infty}^{+\infty} \frac{|E|}{\sqrt{E^2-\Delta^2}} \left[f_l(E) - f_r(E+eV)\right] dE \qquad |E| \geq \Delta \quad (1.36)$$

It is possible to show that, in the limit of zero temperature, the bias voltage dependence of $j_{\mathbf{SN}}$ is given by:

$$j_{\mathbf{SN}} \propto \begin{cases} \sqrt{(eV)^2-\Delta^2} & |eV| \geq \Delta \\ 0 & |eV| < \Delta \end{cases} \quad (1.37)$$

The behaviour of the tunneling current in the two cases is shown in Fig. 1.9a. The different features are more evident plotting the dI/dV curves, i.e. the derivative with respect to the bias voltage V (see Fig. 1.9b).

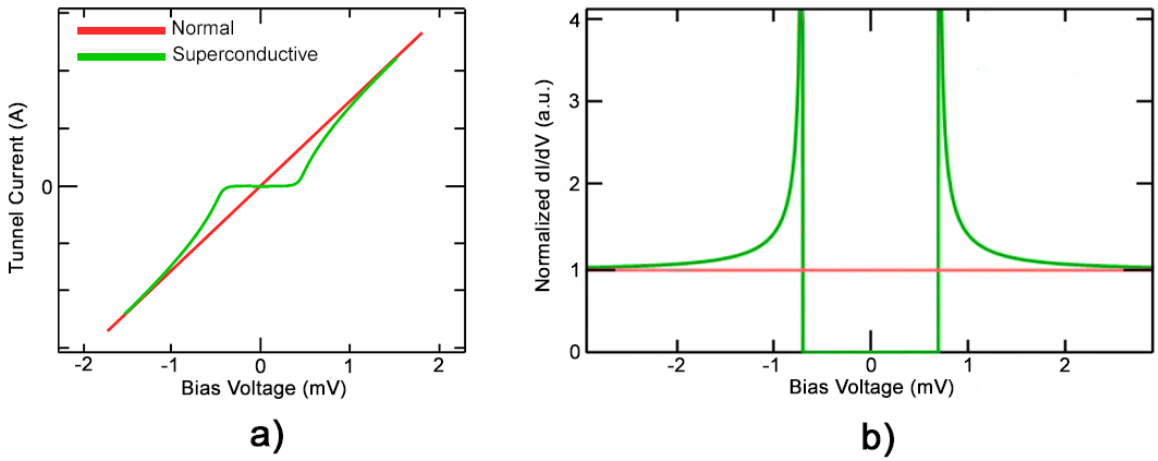

Figure 1.9: I(V) (**a**) and dI/dV (**b**) curves for a Normal-Normal (red) and Normal-Superconductive (green) junction. (b) is taken from [38]

Thus, measuring the tunneling current as a function of the applied bias voltage can be used to obtain information about the microscopic density of states of materials, and to measure the energy gap in superconductors. This type of measurement is the basis of the spectroscopic technique described in Chapter 2.4.2.

Chapter 2

Experimental Techniques

Scanning Tunneling Microscopy presents some major advantages compared to other microscopy techniques, among which the improved spatial resolution and the ability to detect variations of the superconducting condensate of the order of ξ. Magnetic techniques, such as scanning Hall probe microscopy and scanning SQUID microscopy, are instead limited to variation of the order of λ, which is larger than ξ in type-II superconductors. However, in order to perform good STM measurements the sample surface must be as clean as possible, to avoid the tip getting in direct contact with dirt particles that can reduce the quality of the data.
Hence, great importance must be given to the fabrication and characterization of our samples, as defects and impurities play a relevant role in determining the state of the vortices in the nanostructures.

2.1 Choice of the material

A fundamental aspect is the choice of the right superconducting material, to take the maximum advantage from its chemical and physical properties. The first basic requirement is of course being a type-II superconductor, otherwise no vortex state can be observed. Secondarily, the critical temperature has to be in a range than can be easily reached with the experimental setup. In order to observe variation in the vortex configuration, ξ, which is roughly the size of the vortex cores, has to be larger than the STM resolution ($\sim$ 1 nm) and smaller than the maximum scan range of the microscope ($\sim$ 1 μm). Similarly, the superconducting energy gap Δ needs to be larger than the thermal noise at the measurement temperature, or it would be impossible to discriminate between superconducting and normal regions in the sample. Finally, a high degree of homogeneity is essential to reduce the density of defects in the samples, as they act as pinning centers where vortices get trapped, thus modifying the overall configuration.
One material that satisfies all of these requirements was found to be an alloy of Molybdenum and Germanium, the $Mo_{79}Ge_{21}$, where the stoichiometry is optimized to have the maximum critical temperature. Some of the main parameters of this alloy are summarized in Table 2.1.

Previous works have shown that MoGe can form homogeneous amorphous films even at

Bulk critical temperature (T_c)	7.4 K
Bulk superconducting energy gap (Δ)	1.1 meV
Effective coherence length (ξ_{eff})	> 5 nm
Effective magnetic penetration depth (λ_{eff})	18 μm (for a 10 nm film)

Table 2.1: Summary of the main characteristic quantities of $Mo_{79}Ge_{21}$, partially taken from [39].

very low film thicknesses [40].

2.2 Fabrication of the samples

As stated in Chapter 1, the aim of this work is to study vortices in superconductors in a confined environment. To do so, we fabricate superconducting nanostructures whose edges act as a confining potential for the vortices created inside of them. Being interested in geometrical nanostructures, it's necessary to have an optimal control over the edge quality, that can be achieved with modern lithographic techniques. E-beam lithography possesses nanometric resolution and was used in this work to obtain sharp-edges nanostructures.
An overall description of the different steps of the nanostructures fabrication is given in Fig. 2.1.

The procedure can be summarized as follows:

a: Firstly, a layer of PMMA (polymethil methacrylate, a high resolution resist for e-beam writing) is deposited on the insulating SiO_2 substrate;

b: Using Electron Beam Litography (EBL) the nanostructure pattern is written on the resist, which gets damaged by the electron beam. The damaged resist is then removed using a solvent, leaving empty regions corresponding to the lithographic pattern required (developing). The high resolution provided by EBL allows a satisfactory control over the shape and the edges of the nanostructures to be written;

c: A Germanium layer is evaporated on the sample using Molecular Beam Epitaxy (MBE), providing a relatively flat surface where to deposit MoGe. This is done to avoid edge effects that can arise if depositing directly MoGe using Pulsed Laser Deposition (PLD) (see Fig. 2.2);

d: The residual resist is removed via aceton cleaning (lift-off technique);

e: A layer of MoGe is deposited on the sample by means of PLD technique (see Sec. 2.2.1);

f: Gold is deposited via PLD on top of the MoGe film to prevent oxidation of the material, that would make the whole sample opaque to tunneling measurements.

It has to be noted that due to the deposition of MoGe and Au on the whole sample,

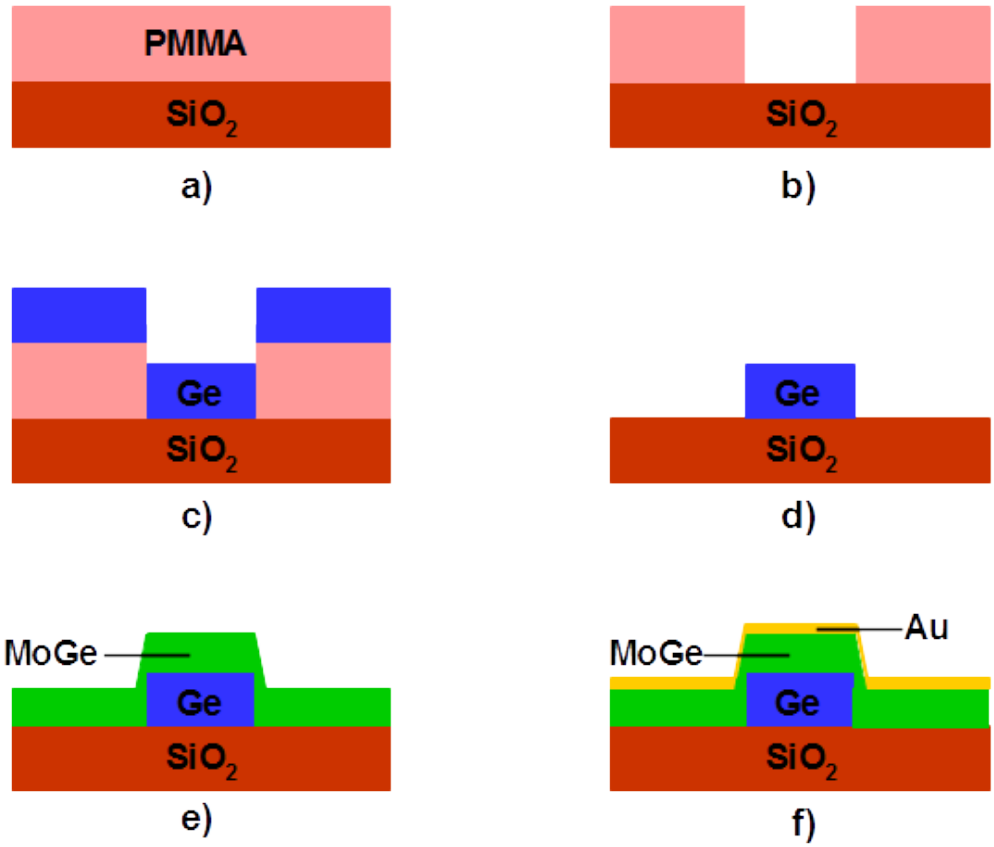

Figure 2.1: Procedure for nanostructure fabrication

there is a weak superconducting link between the nanostructures and the plain film. This is not to be regarded as a problem, because measurements have shown that superconductivity is destroyed in these links by applying a very weak magnetic field, and hence the nanostructures become isolated from the surrounding superconducting film. Each nanostructure is also usually referred to as an "island".
It has also to be remarked that the Germanium layer between the substrate and the MoGe layer is a necessary step in the sample fabrication: because of its high angular dependence, PLD creates huge amounts of deposited material on the edge of the structures if the sample is not flat. This is clearly visible in Fig. 2.2.

2.2.1 Pulsed Laser Deposition

We will briefly describe the technique for the deposition of thin films of MoGe, as part of the thesis work was spent in learning how to grow MoGe and Au films with different thicknesses and roughesses.
Pulsed Laser Deposition is basically a laser-based sputtering technique [42]: a high-power pulsed laser beam is employed to ablate material from a target, and the plasma plume

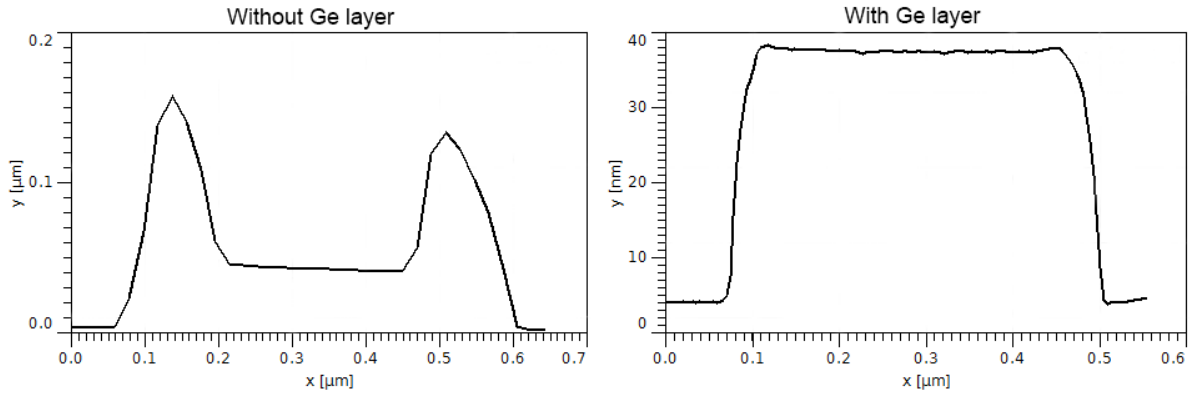

Figure 2.2: Comparison between nanostructure profiles with and without the Germanium layer deposition. These and some of the following images were obtained with Gwyddion software [41].

produced with the ablated species deposits high-energy particles on a substrate, typically placed at a distance between 5 cm and 15 cm, as shown in Fig. 2.3.

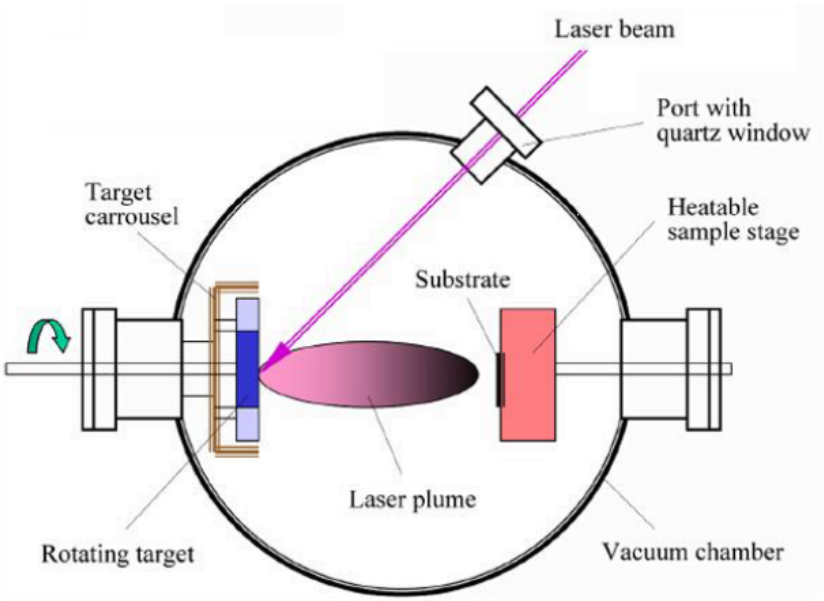

Figure 2.3: Schematic of PLD system, taken from [42]

The laser ablation process starts with photons from the laser pulses, with energy of the order of 100 mJ, that are absorbed on the target usually in a few nanometers. This allows some of the atoms in the absorption region to lose some of their electrons by non-linear processes, es. MultiPhoton Ionisation (MPI). These electrons oscillate in the electric field produced by the laser beam, and in doing so they collide with neighbor atoms, transferring to them part of their kinetic energy. As a consequence of this, the surface of the target melts and the first layers are vaporized, forming the plasma plume that deposits ablated material on the sample. The ablated species have usually enough energy to move to suitable

sites for lattice nucleation. Once the laser pulse is over, the plume dissipates and the front of the target re-solidifies.

Our system is composed of a vacuum chamber, where deposition takes place, and a Nd:YAG laser. Inside the vacuum chamber a multiple target support is used to deposit different materials on the same sample, that is kept at a distance of 10 cm. The sample support can also be heated up to 300°C during deposition, to favor a more homogeneous distribution of the ablated species. A two-stages vacuum system based on a rotary pump and a turbo-molecular pump brings the vacuum down to 10^{-7} mbar, in order to minimize impurities on the sample.
The laser, with a wavelength of 532 nm, produces 10 ns-long pulses at a frequency of 10 Hz. The power of the laser ($\sim$ 100 mW) and the energy of the pulses ($\sim$ 10 mJ) can be controlled and adjusted to obtain the desired deposition rate. Typical deposition rates for our samples are of the order of 1 nm/min.

There are some major advantages in employing this technique for the deposition of thin films: first of all, due to the highly non-equilibrium nature of the technique, the stoichiometry of the target material is conserved in the deposited film, which is of great importance in our case to obtain a homogeneous film of $Mo_{79}Ge_{21}$. This technique also allows for the deposition of a extremely wide range of materials. Being laser-based, PLD can be controlled, and its growth rate modified, by acting on the laser parameters, without changing anything inside of the vacuum chamber. [43].
Among the main disadvantages of PLD, we already mentioned the high angular-dependent distribution of the ablated species. In addition to that, numerous droplets of ablated material (usually $\sim$ 0.5-1 μm high) are deposited on the sample: regions of the sample with a high density of droplets have to be avoided when scanning with an STM tip, due to the chance of crashing the tip if scanning too fast. Optimizing the laser parameters to obtain the desired growth rate while minimizing the amount of droplets is a non trivial task, as the dependence of the deposition rate and density of droplets on the laser parameters (energy of the pulse, frequency, etc.) is quite complex and yet not fully understood.

2.3 Sample Characterization

Once the nanostructures are fabricated, it's important to verify that the whole sample is ready for an STM analysis. This means checking first that the nanostructures are sufficiently similar to one another, so that STM measurements are not dependent on the specific chosen island; it's also useful to control that the thickness is compatible with what is expected from the deposition procedure. Together with this, the quality of the surface in terms of density of defects, droplets and roughness has to be determined. All of these characterization measurements were performed using an Atomic Force Microscope, whose operational principles and main features will be explained in the next paragraph.

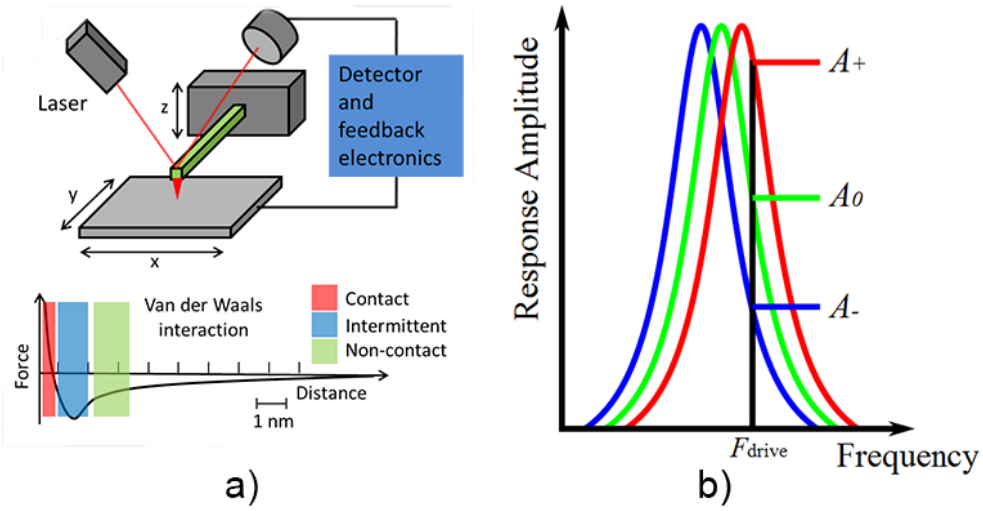

Figure 2.4: **a**: Schematics of AFM system. **b**: Change in resonant frequency due to attractive (blue) and repulsive (red) force, amplitude modulation mode. Taken from [47]

2.3.1 Atomic Force Microscopy

The Atomic Force Microscope (AFM) was developed in 1986 by Binnig, Quate and Gerber [46], a few years after the invention of STM by Binnig and Rohrer. It is composed of a cantilever, usually made of silicon or silicon nitride, with a very sharp tip at its end. When the tip comes into proximity of a surface, forces of different origin (van der Waals, electrostatic, magnetic, etc.) between the tip and the surface set in, leading to a deflection of the cantilever. This deflection is usually measured using a laser spot, that is reflected from the top part of the cantilever into a photodiode, that records its variation. While scanning over the sample surface, a feedback loop typically adjust the tip-sample distance to maintain a constant applied force on the cantilever. This is done by acting on the z-piezo where the sample is fixed, and by recording the signal given to the piezo as a function of the xy position it is possible to reconstruct the topography of the scanned area (see Fig. 2.4a).

A commercial Park Systems XE-100 microscope was used to perform AFM measurements at room temperature and pressure. The system is mounted on an Accurion support that actively reduces ground vibrations, and kept inside a noise-reduction chamber. Images are recorded using the XEP software, and the Gwyddion software is used for image processing and analysis.

There are different operational modes for AFM, according to the nature of the tip motion: Contact mode, Non-Contact mode and Tapping mode. We will focus on the description of the non-contact mode, as that is the one used for our sample characterization. In non-contact mode the tip never touches the surface of the sample. Instead, it is kept at a distance of the order of Angrstroms from the sample. In this tip-sample distance range the dominant force is the attractive electrostatic force between valence electrons and ion cores. These cores become electric dipoles due to the valence electrons in other atoms, so

that the resulting force is a dipole-dipole interaction, the van der Waals force. Being this force relatively weak, it's not possible to measure directly the small deflection of the cantilever. Instead, in non-contact mode the cantilever oscillates near its resonant frequency and the system detects the changes either of the phase or of the vibrational amplitude of the oscillation. These two different procedures are referred to as frequency and amplitude modulation respectively. In our work the amplitude modulation technique was used. With this procedure, the cantilever is excited just off-resonance and is kept oscillating at that frequency. An attractive (repulsive) force acting on the tip will decrease (increase) the resonance frequency, producing a variation in the cantilever oscillation amplitude. This variation is detected using a laser spot, and is used as a reference channel for the feedback loop, to keep a constant amplitude and tip-surface distance (see Fig. 2.4b).

2.4 STM measurements

When it is ready to be measured with STM, the sample is mounted on the head of the instrument. The tip is first coarsely brought close to the sample checking with a magnifying glass to prevent crashing onto the sample surface. Subsequently, an automatic approaching program is used to reach nanometric tip-sample distance.
Once this is accomplished, the system is closed and mechanically isolated from outside vibrations. High-vacuum pressure inside of it are reached using a turbomolecular pump. After this, the whole system is cooled down to a few Kelvin by means of a liquid Helium refrigerator; even lower temperatures, down to hundreds of milli-Kelvin, can be reached using a helium-3 refrigerator. The system is then ready for measurement.
An overview of the operational principles of STM will be first presented in the next section, while in the following one the different kinds of measurements will be described.

2.4.1 Scanning Tunneling Microscopy

The Scanning Tunneling Microscope was developed in 1981 by Gerd Binnig and Heinrich Rohrer [48] at the IBM Zurich, and its discover earned them the Nobel Prize in Physics in 1986 [49]. The underlying physical principle is very simple: a bias voltage is applied between a sharp conducting tip and the sample to be examined, and when their distance is brought to the order of Angstroms a net tunneling current flows (see Fig. 2.5a). This current is a function of tip position, applied voltage and local density of states of both tip and sample. The theoretical aspects of tunneling microscopy have already been pointed out in Chapter 1.2, so we will focus on the experimental aspects.
As the tunneling current depends exponentially on the tip-sample distance, STM can be a difficult technique, as it has to combine an excellent vibration control, very clean sample surfaces and sharp tips to obtain atomic-resolution images. The distance of the tip from the surface, as well as the XY movement of the tip, are usually controlled with high precision by using piezoelectric scans. The whole system is kept isolated from vibration by means of damping systems, combined with a smart design of STM apparatus: for example, if the damping system has a low-frequency resonance value, an STM system with a very high one would be minimally influenced by external vibration.

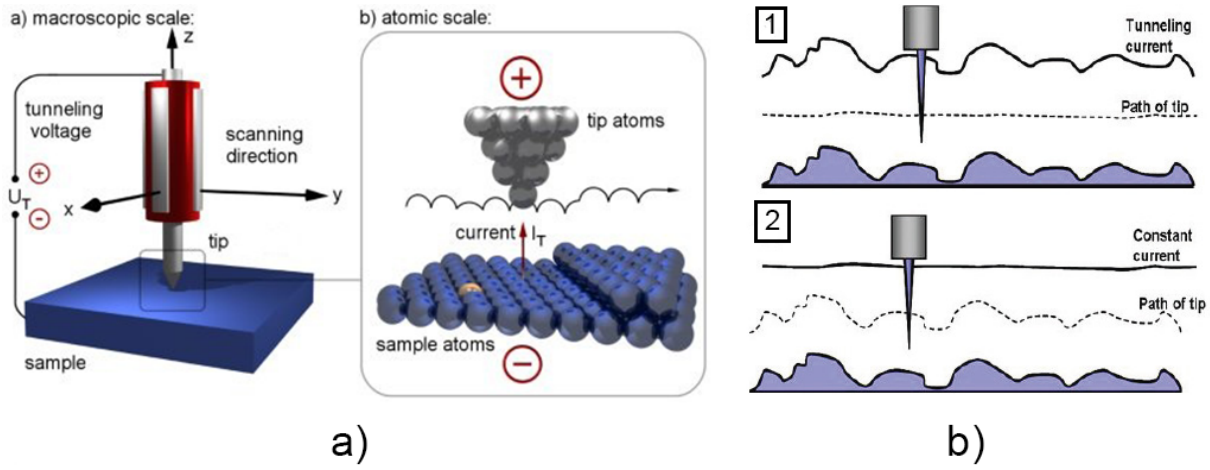

Figure 2.5: **a**: Schematics of STM apparatus, from [50]. **b**: Comparison between Constant Height mode (1) and Constant Current mode (2), from [51].

There are two main modes of operation for an STM, as shown in Fig. 2.5b, which are used depending on the type of measurements to be performed:

- **Constant Height mode:** The tip is kept at a fixed initial distance from the sample surface, and the tunneling current is recorded for every point in the scan. Due to the extreme sensitivity of the current to the tip-sample distance, small variations in the topography will be seen as huge variations in the tunneling current. This method is particularly suited for real-time imaging of dynamical processes on the surface of the sample, such as surface diffusion. A significant drawback of this method lies in the need for almost atomically flat surfaces, whose topographic features have to be smaller than the tip-surface distance. Moreover , the vertical height information (the z-coordinate) is not directly available from the scan, as it is necessary to know the local tunneling barrier height at every point.

- **Constant Current mode:** A feedback loop maintains a constant current between tip and sample by acting on the z-piezo to which the tip is fixed. The feedback signal sent to the piezo can be recorded as a function of the position, and used to reconstruct the topographic image of the scanning area. With this method it's possible to map a complex surface without the risk of crashing the tip into a morphological defect, and for this reason it's the most widely used mode of STM [36].

Our microscope is an Attocube attoAFM/STM system, on which an LTSYS-He3 cooling system is mounted (see Fig. 2.6a). Using a turbomolecular pump the pressure inside the instrument reaches 10^{-6} mbar, and temperature goes down to 300 mK. This is done in two stages. First, temperature is lowered to 4 K thanks to a liquid-^{4}He dewar. At that point the ^{3}He condensation procedure starts: a charcoal sorb is heated to 40 K and releases the adsorbed ^{3}He, which is then condensed by a 1 K plate and collected in the 3-He pot, where it comes in thermal contact with the sample. The charcoal is then cooled to 4 K, and pumping out the "warm" gas allows a further reduction of pressure and temperature,

until reaching the 300 mK range. The ^{3}He gas gradually goes back into the gaseous phase and is collected in the sorb, where the whole cycle can start again.
Two superconducting magnets mounted inside the machine allows to perform measurements with magnetic fields up to 8 T, with accuracy lower than 1 mT. They are kept at cryogenic temperature by the liquid ^{4}He bath. The whole microscope, when operating, is closed inside an insulating container for ground and air vibrations reduction, and is immersed almost totally in the ^{4}He bath.
The STM tip is a gold tip obtained by mechanical sharpening; the bias voltage used during measurements is of the order of mV, and during spectroscopy it is swept between -3 and 3 mV.
Once the system is closed it's impossible to know where the tip is without using a position sensor, that provides a voltage proportional to the distance to the beginning of the sample holder. This sensor has to be calibrated before every closing of the microscope.

Tip and sample are mounted on the STM head, which contains the components needed for sample approach and scanning. As shown in Fig. 2.6b, the tip is attached to the tube scanner, which scans in the xy directions and also moves in the z direction for the fine approach to the sample, to reach the desired value of tunneling current. The tube scanner is

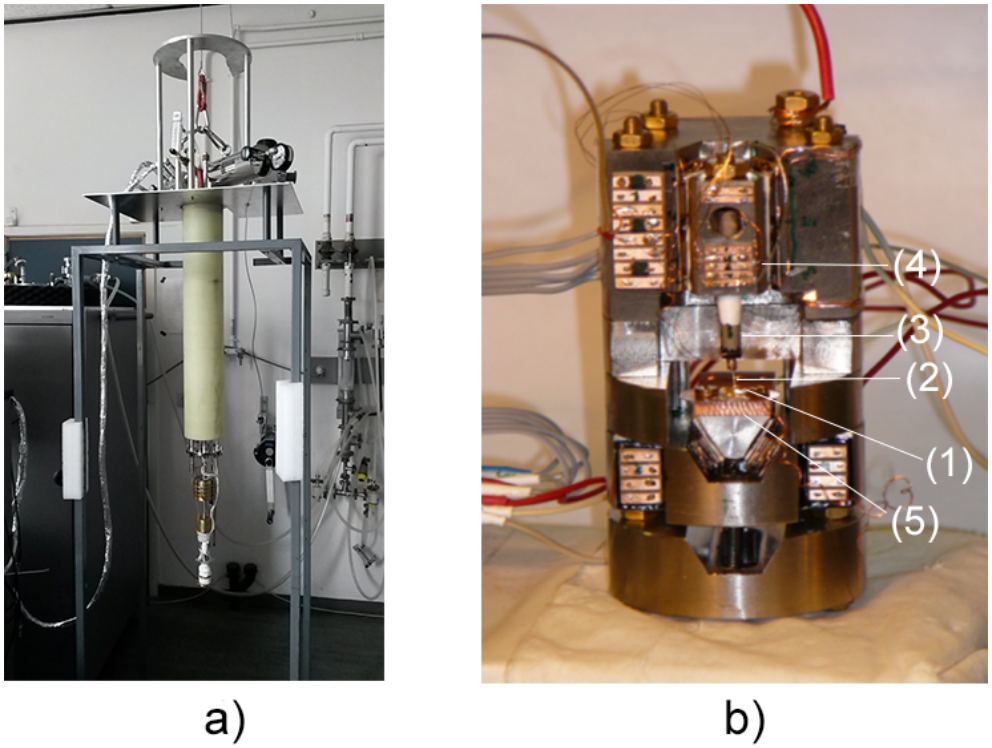

Figure 2.6: **a**: The Scanning Tunneling Microscope while suspended from the ground, before closing it in the insulating container. The support for the STM head (bottom) and some of the tubes of the cooling systems are visible. **b**: Example of STM scan head. (1): Sample holder and magnetic ac coil; (2) STM tip; (3): scan tube; (4): z-piezo tube; (5): x-piezo scanner.

attached to a z-piezo for coarse approach, usually used to reach sub-micrometric tip-sample distance. The sample is attached to a sample holder, around which an ac magnetic coil circles, to provide an additional magnetic field if needed (see Chapter 3.5). Sample holder and coil are fixed to an x-piezo scanner used to move through the sample. A heater and a temperature sensor are also mounted on the STM head.

Images are recorded using the Attocube software Daisy, combined with several LabView routines to perform specific sets of measurements, and processed using Gwyddion.
Scanning Tunneling Microscopy is thus an extremely challenging technique, due to the very low level of external noise required to operate correctly. Any small vibration of the scan head leads to drastic changes in the tunneling current, and eventually to a tip crash on the sample surface, with chance of damaging it. The He dewar refill, to be done every six days, can cause unwanted vibrations in the system, with the risk of losing the island on which the tip is above. Long acquisition times, from minutes to several hours, constitute a major bottleneck of the technique and make it necessary to optimize the time between successive He refills to perform as many measurements as possible.

2.4.2 Types of measurement performed

In this thesis work both Constant Height and Constant Current modes are used to perform different types of measurements. Firstly topographic scans are used to identify a good nanoisland and to bring the tip on top of it. Then, spectroscopic measurements are used to probe the superconducting behaviour of the structure.

Topography scan. Topographic maps allow to know whether the tip is scanning in the vicinity of an island or on a different position, and are used to "navigate" through the nanostructures array. As already explained above, a topographic map is reconstructed from the feedback loop signal which is sent to the z-piezo to maintain a constant current during the scan, as shown in Fig. 2.7a. If the tip is actually on the surface of our sample, it's important to find a good nanoisland where to search for vortex matter: this means discarding those islands where major defects on the surface are present or where the edges are not enough well defined.
Topographic maps are also of key importance in determining the quality of the tip. If the tip is not sharp enough, it won't be able to spatially resolve the sharpest features of the nanostructures, that will appear as more smoothed than they really are. In addition to this, the presence of multiple tips can lead to an identical repetition of some topological features over the map, thus producing a distorted image of the real island (see Fig. 2.7b). Checking for these type of features before performing spectroscopy measurements (see below) is extremely important, and many times the tip quality can be improved reshaping it with short voltage pulses.

Spectroscopy scan. Once a good island has been identified, spectroscopic scans on top of it allow the visualization of superconducting features. A spectroscopic measurement consists of recording the value of the tunneling current at a certain location while the tip is kept at the same distance from the sample and the bias voltage is varied inside a certain,

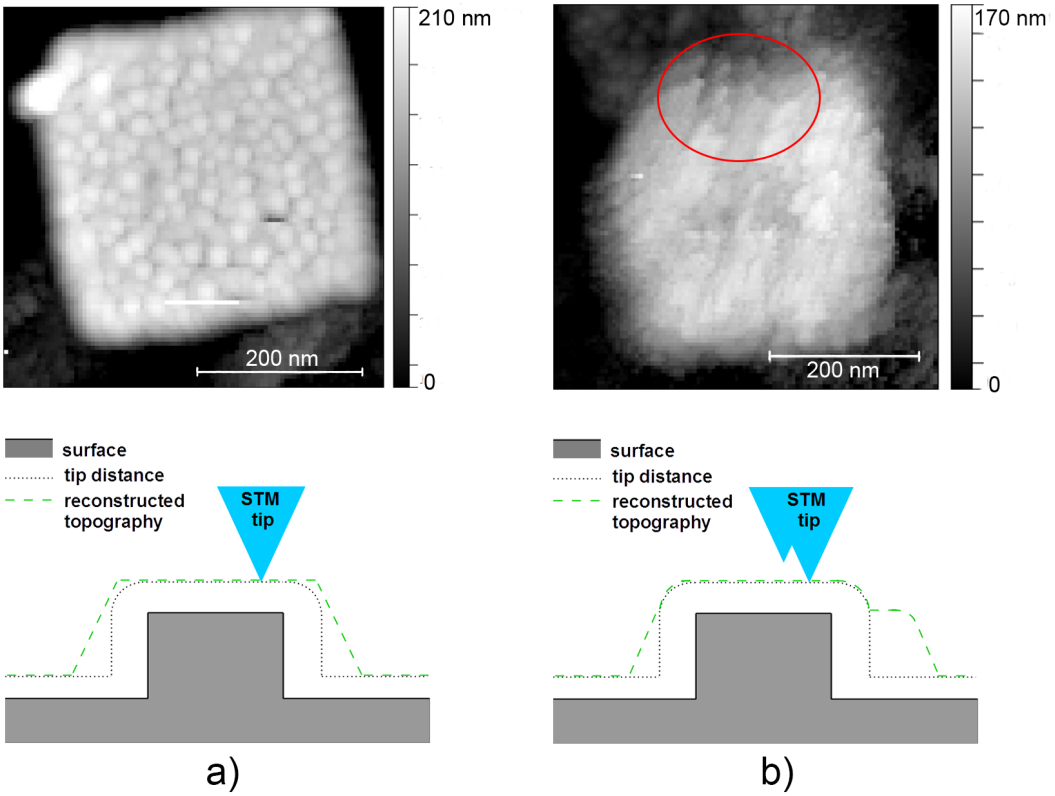

Figure 2.7: **a**: Topographic image of nanosquare done with a single tip. **b**: Topographic image of nanosquare done with a multiple tip. The red circle shows a clear multiple tip feature.

usually symmetrical, interval. The tip is maintained at the same distance by switching off the feedback loop. A spectroscopic map is then a set of I(V) curves of tunneling current as a function of the bias voltage, one curve for every point in the map. This type of measurement is also known as Current Imaging Tunneling Spectroscopy (CITS). As already shown in Chapter 1.2, these curves are substantially different when tunneling from a normal metal (the tip) to another normal metal or to a superconductor (the sample). Thus they can be used to distinguish areas of the sample where superconductivity is suppressed or still present, as shown in Fig. 2.8a. The differences between normal and superconducting regions are even more evident looking at the dI/dV curves, calculated numerically (see Fig. 2.8b). Hence, this type of measurement allows to access directly the local density of states on the sample surface.

An easy way to observe the position of vortices in direct space is then to plot specific values of the dI/dV curves, which are known to be significantly different in N and S zones. A standard choice consists of plotting the Zero Bias Conductance (ZBC), defined as dI/dV(V = 0): when the curves are normalized, ZBC is 1 for a completely normal region and 0 for a completely superconducting one. A Zero Bias Conductance map allows then the direct visualization of the strength of the superconducting condensate and the observation of different interesting features, such as vortex cores, but also screening currents, which are known to reduce the superconducting gap [52].

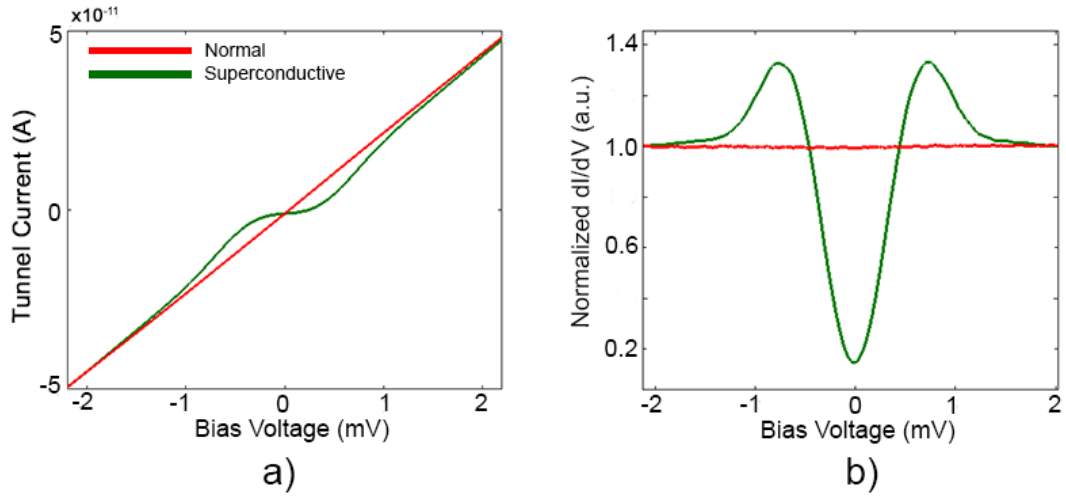

Figure 2.8: I(V) (**a**) and dI/dV (**b**) curves for normal and superconducting regions of the sample clearly show the differen spectroscopic behaviour. Their similarity with the theoretical curves in Fig. 1.9a and 1.9b makes spectroscopy a powerful tool to investigate the superconducting behaviour.

Spectroscopy maps have one main drawback, that is the time for acquisition: a 64 x 64 pixel CITS map can take up to several hours to be done, so that a study of the system behaviour as a function of one parameter (applied magnetic field, temperature, etc.) can be very hard and time consuming. To deal with this, CITS can be used in a different way: instead of recording I(V) spectra for each point in the map with the same parameters, the tip can be kept on a few positions and the spectra are recorded while sweeping the desired parameter. For example, I(V) spectra can be recorded at the center of the island while the temperature is increased in a certain interval.
In this way it's possible to track the evolution of the superconducting condensate as a function of a parameter of the system (B, T , etc.) in a shorter time than measuring complete CITS maps.

Chapter 3

Direct observation of confinement effects in nanostructured superconductors

The aim of this thesis work is to observe the effects of quantum confinement on the vortices produced in type-II superconductors. The chapter is organised as follows:
Section 3.1 deals with the first step of the work, which is the fabrication of the nanostructures and the characterization of sample edges and surface. We are interested in obtaining nanostructures with a well defined symmetry, and a surface as flat as possible.
Secondly, it's necessary to probe the superconducting behaviour of the sample performing spectroscopic measurements on top of it. This is done in Section 3.2. The magnetic field is then switched on, and vortex creation and arrangement is observed on top of the nanoislands. Numerous theoretical works [19] [21] [23] [24] [53] [54] [55] [56] in the past years have outlined the role of sample edges and their geometrical shape in determining the position of vortices in mesoscopic superconductors. A comparison between the theoretical results and the obtained CITS maps is thus carried out. In Section 3.3 further measurements are done to investigate and compare the values of applied magnetic field for vortex entrance and expulsion from different nanostructures.
In Section 3.4 vortex pinning is analysed observing the vortex arrangement in the presence of a pinning center for different magnetic fields. In Section 3.5 measurements regarding vortex entrance in the presence of an additional oscillating magnetic field are shown. They are presented as an open question, as no satisfactory explanation of the observed behaviour has been found so far.

3.1 Sample Characterization

The fabrication process has already been described in Chapter 2. The sample used for this work is a 5x5 mm^2 array of nanosquares, each one measuring 340x340 nm^2 per side. This nanometric size is obtained thanks to the extremely high resolution of the e-beam technique. Being the theoretical coherence length for MoGe smaller than 10 nm, we can consider superconductivity on the islands to be in the strong confinement regime. Each

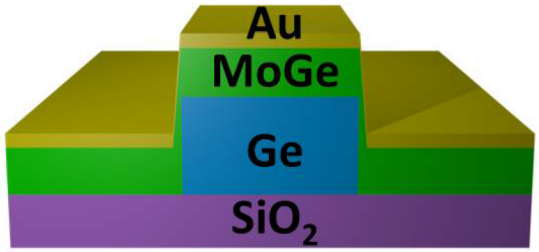

Material	Thickness
Au	5 nm
MoGe	17 nm
Ge	30 nm

Figure 3.1: Sample cross section and thickness of the different layers.

island is composed of a 30 nm film of Ge, on top which 17 nm of MoGe and 5 nm of Au are deposited. The structure is surrounded by a plain film of MoGe and Au of equal thickness. The substrate for both islands and plain film is SiO_2. A schematics of the sample structure is shown in Fig. 3.1.

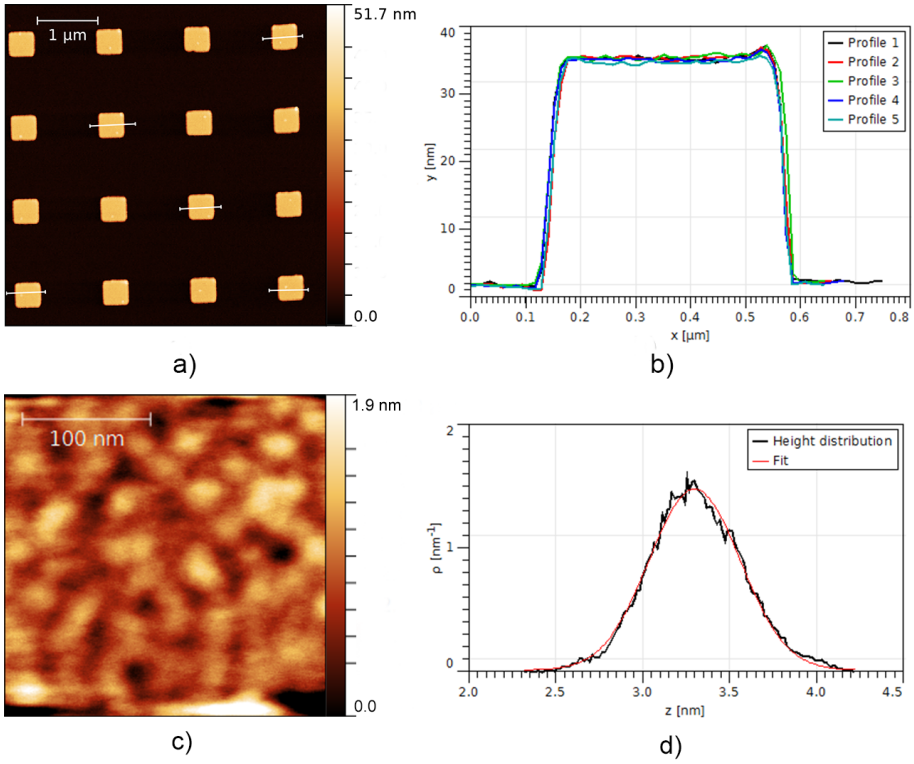

Figure 3.2: **a**: 6 x 6 μm^2 AFM image of an array of nano-squares. The white lines are the profiles traced in (b). **b**: Height profiles of different islands. The excellent superposition of the curves indicates uniformity of deposition among the islands. **c**: 0.25 x 0.25 μm^2 AFM image of an island surface after deposition. **d**: Histogram of height distribution of the scanned area. The dispersion (2σ) of the gaussian curve is used to determine the roughness of the sample.

AFM is used to check the sample quality before introducing it into the STM. In Fig.

3.2a an array of nanosquares identical to the one used for the STM analysis is shown: the different islands present some minor inhomogeneities, mainly due to excesses of deposited material (the white spots visible in some of the squares), but for the purpose of our work we can assume that the sample is composed of approximately identical nanosquares. The similarity between different islands is even clearer looking at Fig. 3.2b, where height profiles have been drawn for five different islands.
The high resolution AFM images allow also to study the roughness of the islands' surface by reducing the scan area to fractions of micrometers, as shown in Fig. 3.2c. One possible way to estimate the roughness is taking the dispersion of the height distribution histogram of each image assuming that it has a gaussian profile (see Fig. 3.2d).
By comparing surfaces both on and off the islands and both before and after the MoGe and Au deposition, it was found that the roughness increases after the deposition when depositing on the SiO_2 substrate, and it remains the same when depositing on the Ge substrate, i.e. on the islands. In the latter case, the roughness is estimated to be around 0.5 nm (2σ of the gaussian), providing a sufficiently flat surface for the STM analysis.

3.2 Probing the superconducting condensate

Once the sample has been correctly mounted inside the STM and a good island has been found, it's necessary to investigate its superconducting behaviour.

This means measuring the current spectra all over the island surface, to verify the homogeneity of the condensate, and so of the density of Cooper pairs. A ZBC map in the zero field state is shown in Fig. 3.3a. Comparing it with the corresponding topographic map presented in the inset, it can be noticed that small inhomogeneities in the condensate

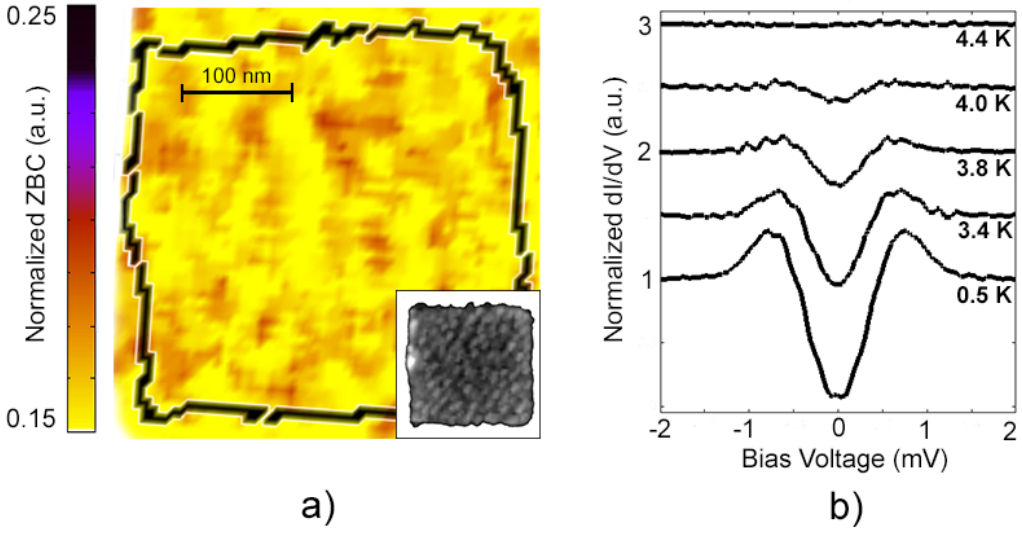

Figure 3.3: **a**: Zero Bias Conductance map of a complete island at T = 0.5 K and zero applied magnetic field. In the inset the corresponding topographic map is shown. **b**: Normalized conductance at a fixed position of the island as a function of tip-sample voltage and temperature.

cannot be linked to the quality of the film or to topographic features. This is important to show that, although the MoGe/Au bilayer is granular, the condensate across the nanoisland is almost uniform.
The superconducting energy gap Δ can also be determined, by fitting the spectra with a function such as Eq. 1.36. Even if the correct absolute value of Δ cannot be determined, as explained in the next paragraph, this parameter is the characteristic feature of tunneling phenomena in a superconducting state, and is thus used as an indicator of the strength of the superconducting condensate.
This can be seen in Fig. 3.3b, where a gradual transition between a superconducting and a normal state is shown by plotting the dI/dV curves as a function of the bias voltage for different temperatures: the distance between the peaks, which is linked to the gap value (recall Eq. 1.36 and Fig. 1.9), is observed to reduce until disappearing in the fully normal state at 4.4 K. From transport measurements, the expected T_c for a 17 nm thick film of MoGe is around 6.2 K. The observed reduction of T_c is due to the presence of the 5 nm of Au on top of the sample.
Before proceeding further with the presentation of the results, it is then necessary to take into account how the Au layer influences spectroscopic measurements.

3.2.1 The Proximity Effect

Depositing a thin layer of Au (a non-superconducting material) on top of the nano-islands is an unavoidable step in our sample fabrication process. Without it, a $\sim$ 2.5 nm thick oxide layer would form on top of the MoGe film, and tunneling through that barrier would be extremely hard. When a superconductor (S) and a normal metal (N) are put in good electrical contact, there is a finite-length region at the interface where Cooper pairs from S diffuse through the N region, losing their coherence and finally unpairing. Because of this, part of the metal close to the interface S becomes a superconductor, with a T_c and a density of Cooper pairs n_s that decrease exponentially with the distance from the NS interface [44]. This effect is called "proximity effect", and it explains how superconductivity can be observed with STM through a thin metallic layer.

We will not focus on the analytical treatment of this rather complex phenomenon, but only underline some aspects to be taken into account for our STM analysis:

- A very thin Au layer in contact with the MoGe film possesses superconducting properties, as there is a non-zero density of Cooper pairs inside of it. In other words, the order parameter is lower than in a real superconductor, but larger than 0 (see Fig. 3.4a). Due to diffusion of both electrons and Cooper pairs through the gold layer, the observed vortex core size will be larger than the real one, even if its position is not expected to change, as shown in Fig. 3.4b.

- Experiments have been carried out by the research group to show how the overall vortex configuration is not modified by the presence of a thin Au layer, using bulk $NbSe_2$ instead of MoGe. As shown in Fig. 3.5a, the Abrikosov lattice arrangement is clearly visible through the gold layer, indicating that the position of vortices is preserved by the uniform electron diffusion.

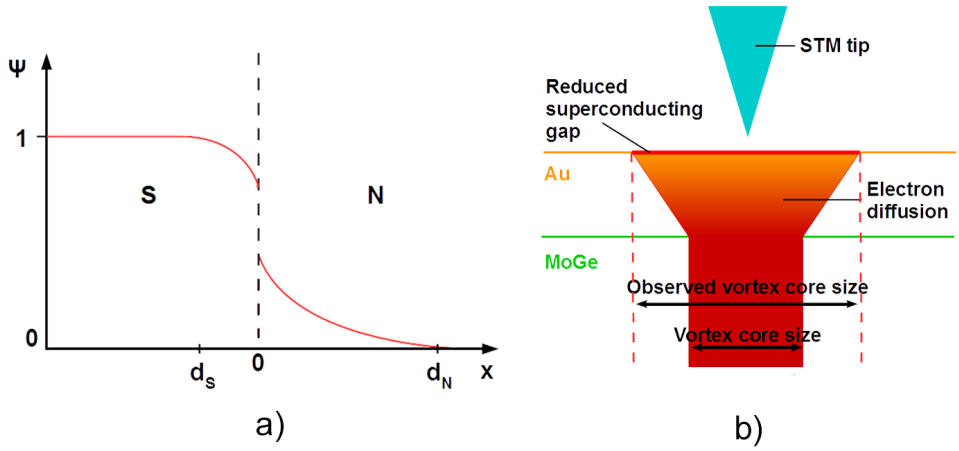

Figure 3.4: **a**: Behaviour of the order parameter at the interface between a superconductor (S) and a metal (N). d_N and d_S are the characteristic lengths in N and S over which the order parameter changes. **b**: Schematics of how the proximity effect can change the size of vortices but not their position.

- In the Au layer ψ has a smaller value than in MoGe, which means that superconductivity is destroyed in the metallic film at a temperature $T_c^* < T_c$. For an analogue reason the superconducting energy gap Δ^* measured with STM is lower than the proper Δ in the superconductor (see Fig. 3.5b). Hence, quantitative measurements of parameters of the superconductor (T_c, Δ, ξ etc.) via STM should take into account

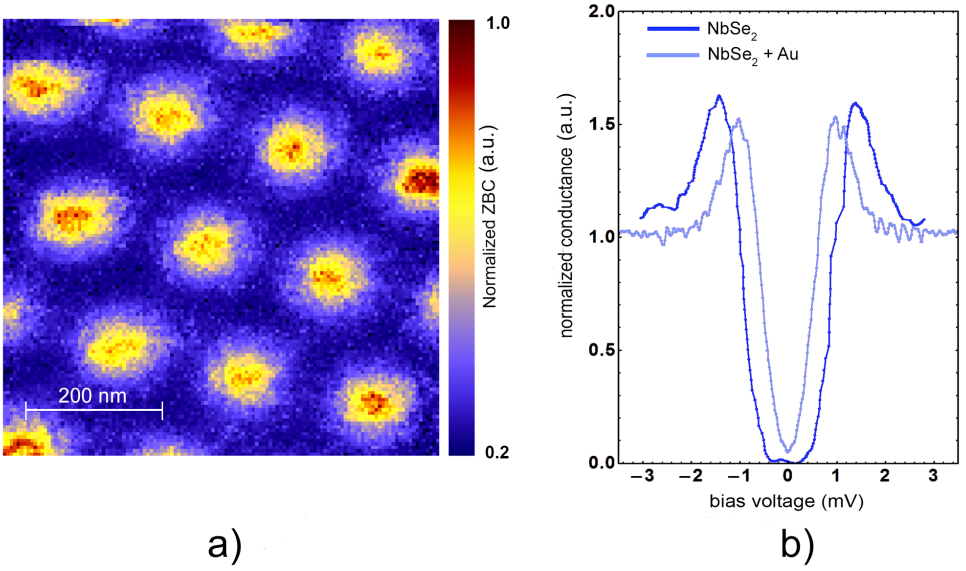

Figure 3.5: **a**: Zero Bias Conductance map of $NbSe_2$ covered with 5 nm of Au. The Abriksov lattice arrangement is clearly preserved through the metallic layer. **b**: dI/dV spectra for $NbSe_2$ with and without the Au layer. In the first case the spectrum doesn't reach 0 at 0 mV, and the gap is reduced compared to the case without Au

this "filtering" effect due to the gold layer.

To summarize, the Au layer only modifies superconductivity by uniformly weakening it across the island, and at the same time it prevents oxidation. Without a more detailed analysis of the effect, we can say that the MoGe/Au structure allows us to investigate via STM the influence of sample geometry on the superconducting parameters of MoGe.

3.2.2 Imaging the vortex state

When switching on the magnetic field, screening currents start to run around the borders of the island, to keep the magnetic field out of the nanostructure. It was shown in numerous works, for example in [57], that the process of vortex entrance takes place when the density of Meissner currents approaches the depairing value j_D, which would destroy superconductivity. The vortex state can be visualized with CITS maps (see Chapter 2.4.2) by plotting for example the Zero Bias Conductance as a function of the xy position. Normal regions such as vortex cores and defects will have ZBC values close to 1, while fully superconducting regions will show a ZBC around 0.2 (not exactly 0 because of the proximity effect).

Screening currents can be visualized as well, because they reduce the superconducting

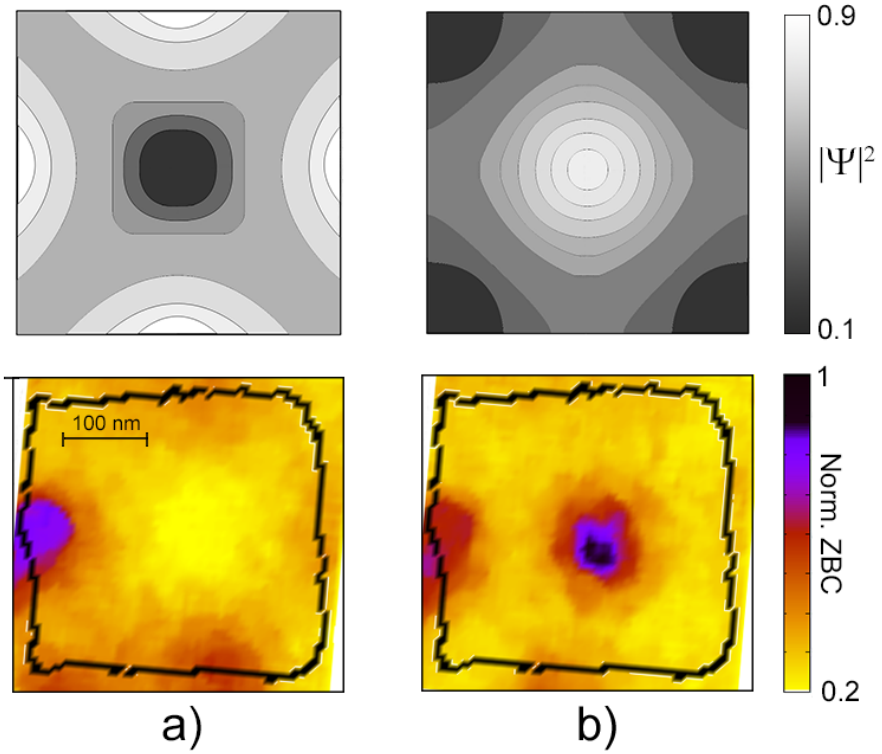

Figure 3.6: Comparison between expected Cooper pairs density (schematics based on [58]) and observed ZBC distribution in the L = 0 (**a**) and L = 1 (**b**) states. Regions of depleted superconductivity on the edges are due to the higher density of screening currents. L = 0 state is measured at 50 mT, L = 1 at 60 mT.

gap by locally increasing the kinetic energy [52]. By observing simulations (ref) the density of supercurrent is larger at the edges, and Cooper pairs there possess an additional kinetic energy. If that energy was larger than the condensation energy, the pair would break and superconductivity would be locally destroyed. At smaller values of kinetic energy, the superconducting state is preserved, but the superconducting gap is reduced, as a smaller amount of energy is required to break the pair. This means that screening currents can be observed as regions of reduced gap (higher ZBC) in CITS maps.

This is shown in Fig. 3.6, where ZBC maps of an island just before and just after the entrance of the first vortex are presented, and compared to expected distributions of the order parameter. The black squarish line inside the scan area represents the topography contour of the island. In the L = 0 state (Fig. 3.6a), strong screening currents circulate along the edges of the square, resulting in a higher value of ZBC compared to the center. When the supercurrent density reaches the depairing value j_D, superconductivity is locally destroyed and a vortex is allowed to enter the sample (Fig. 3.6b). The vortex places itself at the center of the square, and on the borders screening currents are strongly reduced. This happens because the total kinetic energy of the supercurrents in the L = 0 state equals the sum of the kinetic energy of the currents in the L = 1 state plus the condensation energy of the vortex core. This brings a significant decreasing of screening currents in the L = 1 state.
On the left edge a defect is visible as a region of depleted superconductivity, and despite its presence the symmetric arrangement of vortex and screening currents is still clearly visible.

Increasing further the magnetic field leads to the entrance of more vortices in the island, and the overall arrangement will be determined by the interaction of vortices with the edge of the nanostructures.

3.2.3 Symmetry induced configurations

Several theoretical works regarding vortex arrangement in nanosquares provide a large amount of predictions that can be compared with our experimental results. Simulations on symmetry induced configurations have been carried out by numerically solving the Ginzburg-Landau equations (Eq. 1.11 and Eq. 1.12) with specific boundary conditions that reflect the specific geometrical problem under consideration. Estimates on the magnetic field values for each vortex entrance are obtained by calculating the free energy at different vorticities L as a function of the applied magnetic field. When the free energy at vorticity L+1 gets smaller than the one at vorticity L, a new vortex has entered. This can also be seen by plotting the magnetization as a function of the applied magnetic field: at every vortex entrance **M** will experience a sudden drop, due to the additional magnetic flux quantum inside the sample, as already shown in Fig. 1.6d.

To observe the arrangement of vortices in the structure, the Cooper pairs density can be plotted as a function of the position, at a specific magnetic field: vortex cores will naturally appear as regions where Cooper pairs density is strongly reduced. Simulations on square samples have shown that the expected configuration for states at low vorticity follows the

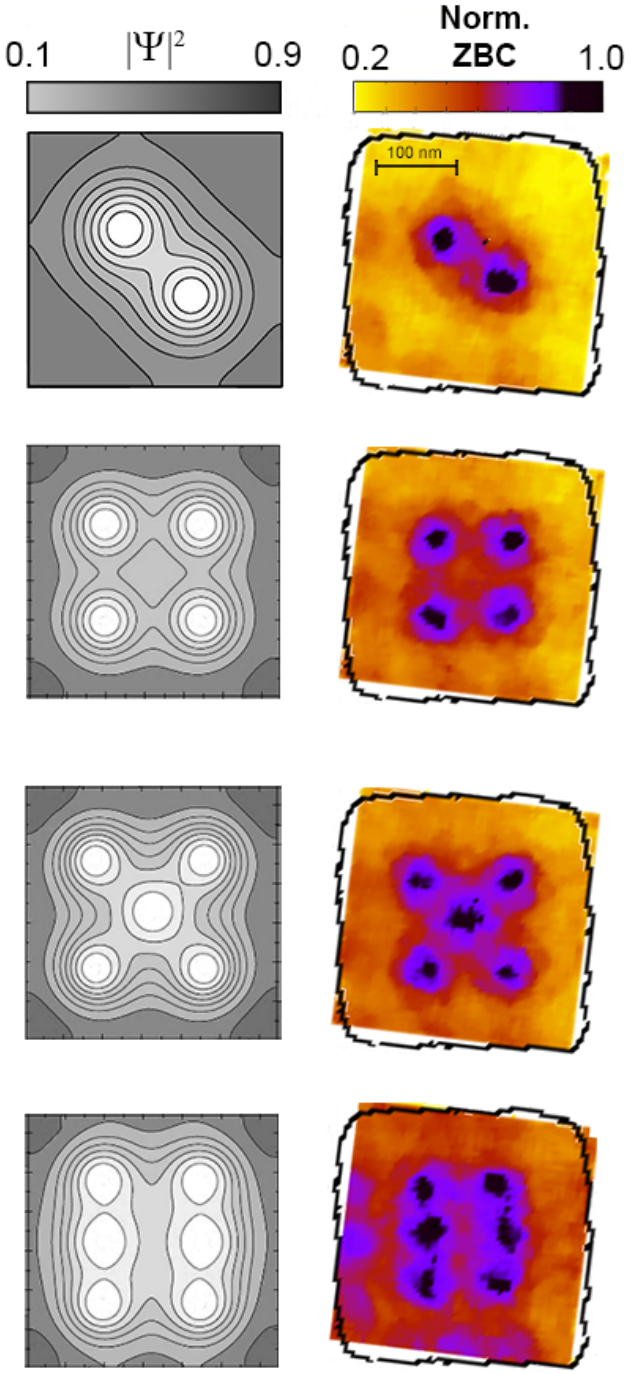

Figure 3.7: Comparison between simulated data from [19] and [55] and ZBC maps obtained via STM for the L = 2, 4, 5 and 6 states. All of the vortex patterns follow a C_4 symmetry, and the agreement between theory and experiment is excellent. The CITS maps are recorded at 75 mT, 115 mT, 130 mT and 180 mT, from top to bottom.

geometrical boundaries imposed, namely a four-fold rotational symmetry [19] [22] [55].
This behaviour has already received experimental confirmations [16] [17], but mainly using magnetic techniques, which could resolve the configuration only at the penetration depth scale. No experimental work has shown vortex arrangement in mesoscopic squares via Scanning Tunneling Spectroscopy, which allows to resolve the variations of the superconducting condensate at the coherence length scale.

States with different L are experimentally investigated performing CITS maps of the whole surface of an island at increasing values of applied magnetic field. Plotting the normalized Zero Bias Conductance allows a direct comparison between our results and the simulations, as shown in Fig 3.7. Experimental and theoretical data show an excellent agreement, especially if we recall that simulations are carried out on perfectly symmetric squares, while the measured islands always present a small degree of inhomogeneity. This shows how symmetry is the leading factor in determining the vortex arrangement. To our knowledge, this is the first direct confirmation of the predicted, symmetry induced vortex distribution in superconducting nanostructures using STM.
It's important to notice that the surface of the islands has to be as clean and smooth as possible, as any defect or impurity can change significantly the vortex arrangement, as described in Section 3.4.

3.3 Vortex entrance and expulsion fields

While CITS maps are used to visualize vortex states when system parameters are held fixed, a different spectroscopic approach is needed when we are interested in the system behaviour while sweeping, for example, the applied magnetic field or the temperature.

As islands obtained by lithographic techniques can present some minor differences, it's

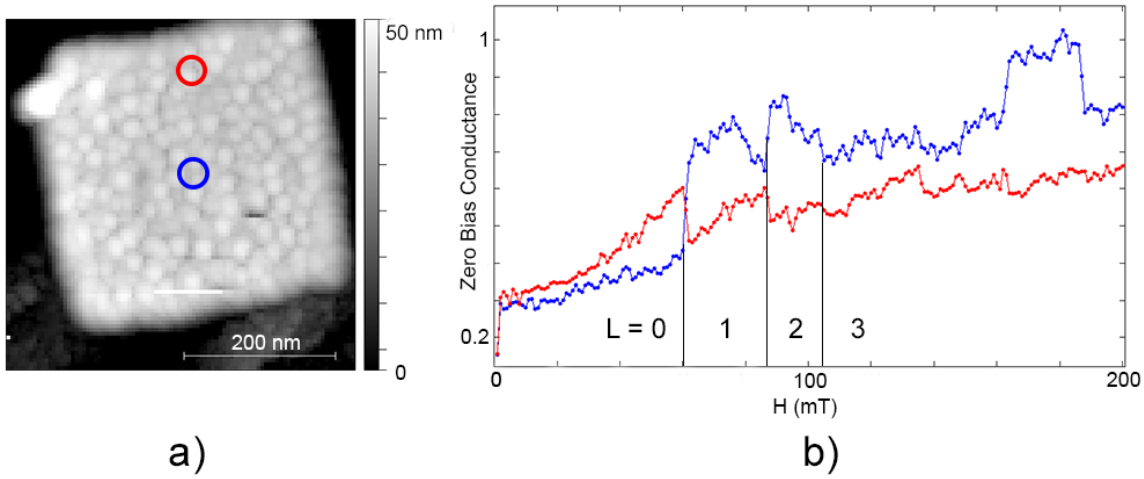

Figure 3.8: **a**: Spectroscopy is carried out on the two positions encircled in blue and red. **b**: Zero Bias Conductance as a function of the applied magnetic field for the two different positions. The first three vortex entrances are indicated with a black line.

important to verify that these differences don't alter significantly the superconducting properties among the islands.
Instead of recording spectra in every point of the scanned area, for this set of measurements the tip is placed at a few chosen locations on the island, and spectroscopy is performed at different values of the sweeping parameter. In this way the spectra are acquired in a shorter amount of time, allowing also a comparison between different islands.
In this work we observed the change in vortex pattern while sweeping the magnetic field H, placing the tip at the edge and at the center of the nanoisland (see Fig. 3.8a), and observing the changes in the Zero Bias Conductance curves. In the L = 0 state, when increasing H, no significant changes are visible in the ZBC curve in the center, while the curve taken on the edge starts to grow, as superconductivity is weakened because of the onset of screening currents. When the first vortex enters, it places itself in the center of the square, while screening currents experience a sudden decrease: this situation corresponds to a sharp increase of ZBC at the center, and a decrease of ZBC at the edge. In this way the exact value of H for the first vortex entrance can be extracted. Increasing H further, several other sudden changes in ZBC can be traced, corresponding to new vortices entering the island, as shown in Fig. 3.8b. The same procedure is then performed while decreasing H until 0, obtaining the expulsion field values for the different vortices. A schematics of the evolution of screening currents in the passage between L = 0 and L = 1 states is presented in Fig. 3.9a for a circular island.

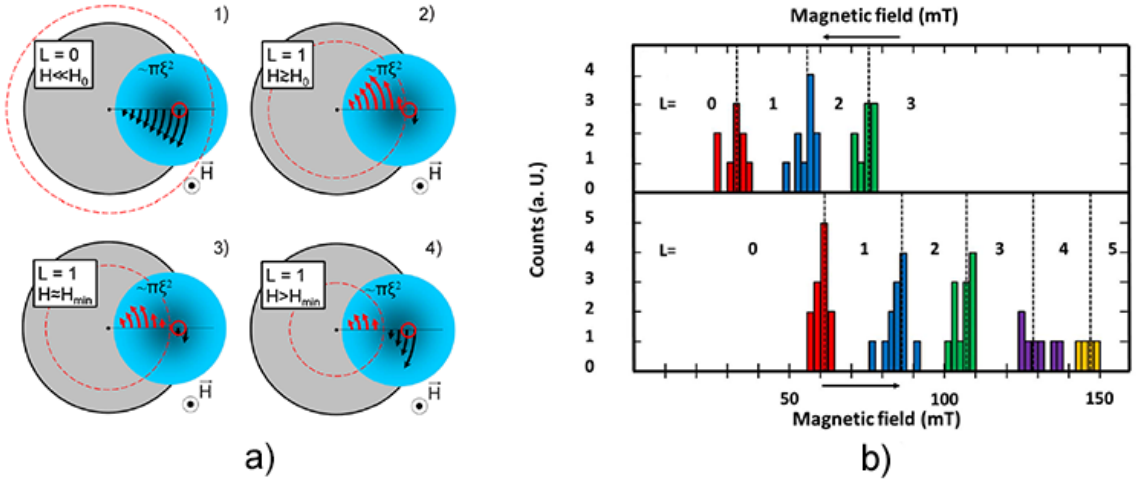

Figure 3.9: **a**: Schematic drawing of competition between screening currents (black arrows) and vortex currents (red arrows) at increasing applied magnetic field H. The small red circle shows the fixed position of an imaginary STM tip on the edge of the sample. Taken from [52] **b**: Magnetic field values for the transition between different L-states for increasing (down) and decreasing (up) H. Same colours relate the same steps in vorticity, and hysteresis is clearly visible.

These measurements were done on several islands, and the magnetic field values corresponding to the different vortex states were compared on a histogram, as shown in Fig. 3.9b. In general all transitions happen at similar values of the magnetic field, indicating that

at first order the different squares have similar superconducting properties. Nevertheless, a spread around each value is clearly visible, indicating that small defects and imperfections play a role in determining when the system shall change its state.
In addition to this, the values for vortex expulsion are relevantly smaller than those for vortex entrance, for the same number of vortices, indicating a strong hysteresis that is typical of magnetic flux trapping [59]. While the system is in the Meissner state it is characterized by a reversible magnetic response, whereas in the presence of moving vortices energy dissipation leads to an irreversible behaviour. Several mechanisms contribute to this hysteretic behaviour, and we will just briefly summarize two of the most relevant ones.
Firstly, as already stated in Paragraph 3.2.2, in order for the first vortex to enter the island, the screening currents on the edges have to reach the depairing value j_D, which leads to a local destruction of superconductivity. The presence of normal regions in the nanosquare is a source of energy dissipation, and the complete reversibility of the previous Meissner state is lost. The required magnetic field to allow the entrance of the first vortex is then H_{jD}, which is predicted [60] [61] [62] to be slightly larger than the lower critical field obtained from GL theory. On the contrary, for vortex expulsion no depairing current on the edges is needed, resulting in a difference between entrance and expulsion magnetic field values.
Secondly, the surface of each islands provides an energy barrier that each vortex has to overcome to enter and exit the structure. As described in the work of Bean and Livingston [63], in a bulk superconductor the surface contributes to the total energy of the system with a barrier close to the edges, which prevents the entrance of a quantum of magnetic flux until a field $H = H_{BL} > H_{c1}$ is reached. This barrier results from the interplay between an attractive force between surface and vortex, due to the requirement of zero current normal to the surface, and a repulsive one caused by the screening currents running around the surface. In the same way, the expulsion of the magnetic field happens at a lower field than H_{c1}, resulting in a hysteretic cycle for the magnetization of the sample.

3.4 Vortex Pinning

As already mentioned in Chapter 2.1, the presence of defects such as grain boundaries or hillocks of deposited material can trap vortex cores in their neighbouring and prevent them from moving when an external force is applied, a mechanism known as pinning [64]. Understanding vortex pinning is hence a necessary step towards the development of practical technologies for dissipationless current transport.
There are numerous mechanisms responsible for vortex pinning, and they are usually divided between core-pinning and electromagnetic-pinning. Core-pinning happens when topological or structural defects bring to a partial reduction of superconductivity (i.e. of the order parameter) on a local scale. This brings to an increase in the total energy of the system by the amount required to break part of the Cooper pairs in that region. For a vortex core, which corresponds to a region of size ξ of strongly reduced superconductivity, it is energetically more favourable to place itself close to the defect. Indeed, the total amount of additional energy will be lower in this case rather than if vortex and defect were far away from each other (see Fig. 3.10a).
Electromagnetic pinning is due to the interaction between the kinetic energy of the screening currents around the defect and the perturbation of the vortex magnetic field. From a

theoretical point of view the interaction can be described by assuming the presence of an antivortex images on the pinning site [65]. The result is that the pinning center act as a so-called antidot, attracting vortices to its position[66]. This explains why a vortex, when pinned on a defect, will try to maintain its position if the applied force on it is not too strong.

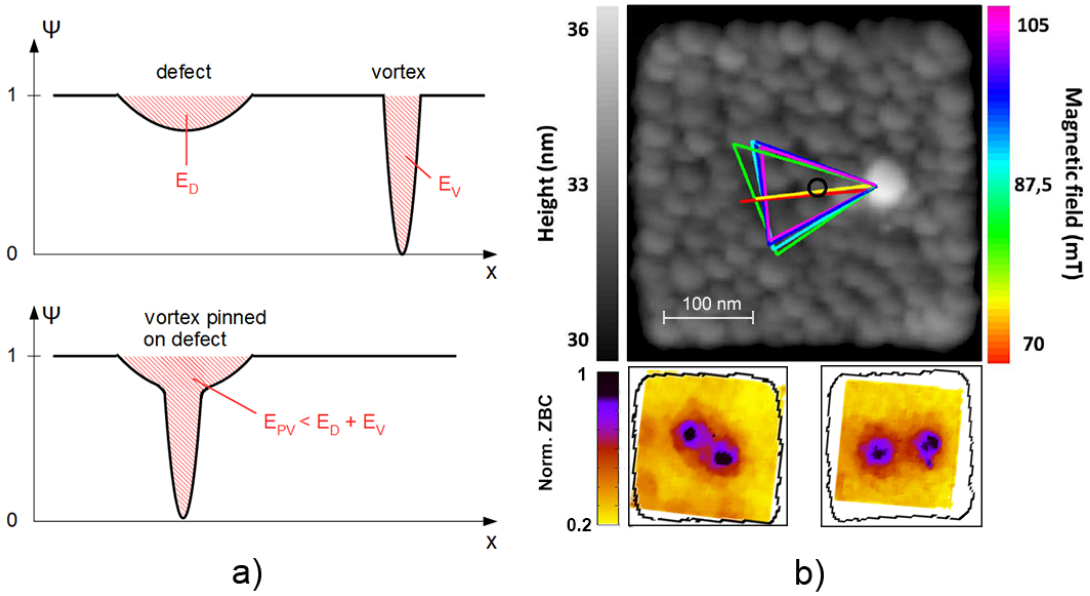

Figure 3.10: **a**: Schematics of vortex pinning as an energetically favourable process. **Top b**: Topographic image of an island with a hillock close to the center. The circle, lines and triangles stand for one, two and three vortices respectively, and the different colors represent different applied magnetic fields. **Bottom b**: CITS maps of a "clean" (left) island at 75 mT and of the one on Top b (right) at 72 mT in a two-vortex state.

By selecting an island with a clear defect on its surface, we were able to study the behaviour of vortices in the presence of a pinning center. In Fig. 3.10b the topography of the island is shown, on top of which the positions of vortices are traced as vertices of a line (two vortices) and of a triangle (three vortices): a single vortex (black circle) places itself in the center, being not affected by the presence of the defect; when the system enters the two-vortices configuration, one of the two is pinned on the defect, while the other one moves with increasing magnetic field. When the third vortex enters, only the non-pinned ones change their positions. A comparison of ZBC maps of a two-vortex state with and without a pinning defect shows an evident modification of vortex configuration: without any defect the two vortices arrange themselves along one of the diagonals, as predicted by theory, while in case of pinning the arrangement is significantly different.

3.5 Open question: Response to an oscillating magnetic field

In the last part of the experiment we investigated how the barrier for vortex entrance and expulsion can be modified if a small oscillating magnetic field is superimposed, in the same direction, on the static magnetic field needed to create vortices. Ac measurements like these can help exploring how the process of vortex nucleation takes place, and what are the main parameters influencing it. More generally, understanding the behaviour of type-II superconductors in the presence of an oscillating magnetic field is a necessary step for the development of specific superconducting devices.
The additional magnetic field is obtained by injecting a sinusoidal current in a small coil encircling the sample. This excitation can lead to an earlier entrance of the vortex inside of the sample, when the static magnetic field is a few mT lower than the expected value for vortex nucleation. It's interesting to notice that, with currents of the order of a few mA and frequencies up to 1 kHz, the increase in magnetic energy due to the AC field is estimated to be equivalent to an increase of ~ 0.1 mT of the static magnetic field. Hence, the early entrance cannot be explained simply as an increase of the average applied H, but it has to deal with the oscillating nature of the excitation.

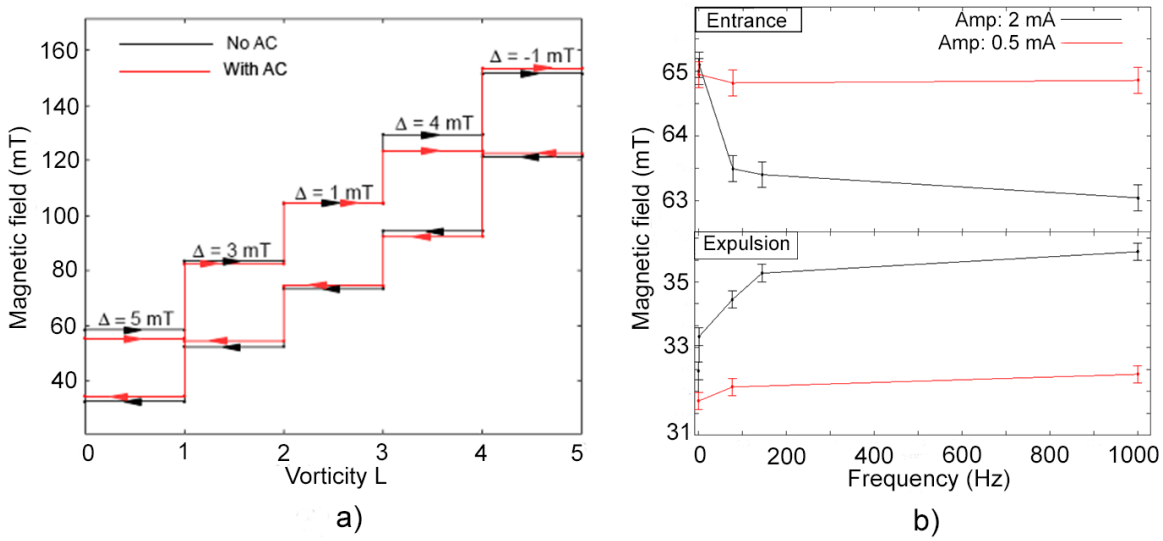

Figure 3.11: **a**: Part of magnetization cycles without (black) and with (red) an AC magnetic field, with amplitude 4 mA and frequency 77 Hz. Hysteresis is slightly reduced in the second case in almost all considered L-transitions. Above each step the difference in total hysteresis is showed. **b**: Frequency dependence of the first vortex entrance (top) and expulsion (bottom) field value at two different amplitudes for the AC modulation. Both the fast change at low frequencies and the saturation for high frequencies are visible.

Data were acquired by performing spectroscopy measurements on a line of points passing through the center of each island, and then observing the Zero Bias Conductance distribution along the nanostructure as a function of position and magnetic field. Transitions between different L-states were visible as discontinuities in the ZBC distribution.

A first effect that was observed when applying an AC magnetic field is a reduction of the hysteresis in the magnetization cycle, estimated as the distance between the expulsion and entrance fields between the same vorticity states, as shown in Fig. 3.11a. Δ indicates the difference in hysteresis between the No Ac and With Ac cases. The additional field "helps" vortices to overcome the energy barrier that prevents them to enter and exit the sample, but how this is physically carried out, i.e. the interaction between the barrier and an oscillatory magnetic excitation, is not clear yet.
The role of frequency and amplitude of the oscillation was then investigated, to observe how the two parameters separately influence the system behaviour. We limited ourselves to the analysis of the first vortex entrance/expulsion to reduce the acquisition time. Performing successive measurements with same frequency and increasing amplitude indeed showed a modification of the entrance field, but the limited amount of data didn't allow the observation of a definite dependence on amplitude.
On the contrary, keeping the amplitude constant and sweeping over the frequency showed a more reproducible behaviour of the vortex entrance field, visible in Fig 3.11b. In a small-frequency range (between 0 and $\sim$ 100 Hz) the magnetic field value is observed to change very fast, with decreases (increases) up to 2 mT for vortex entrance (expulsion). When increasing the frequency further (up to 1 KHz) the field value shows a much smaller variation, which indicates a possible saturation for very high frequencies. In addition to this, both the fast change and the saturation are proportional to the applied current amplitude. The error is estimated as the standard deviation over a set of multiple measurements performed once for one magnetic field value. Again, the origin of this frequency dependence has not been clarified yet, and requires further analysis and a comparison with theoretical models. It is already possible to exclude an effect due to the temperature increase occurring when switching the AC field on, as the temperature dependence has been separately studied and it's not possible to observe a comparable behaviour of the vortex field entrance value.

Chapter 4

Conclusions

In this thesis work we observed the behaviour of magnetic vortices in a strongly confined regime using Scanning Tunneling Microscopy. We performed a first of its kind exploration of lithographically designed nano-structures of MoGe/Au bilayers, and we were able to confirm with excellent agreement theoretical predictions on vortex arrangement in mesoscopic squares. In doing this, we outlined the relevance of the sample symmetry in determining vortex arrangement.
Small variations among different islands, which are unavoidable in this type of sample fabrication, were shown not to alter significantly the overall configuration, only producing small dispersions on the magnetic field values for vortex entrance and expulsion. However, small inhomogeneities and defects allowed us to investigate in greater detail the effects of pinning in nanostructured superconductors. Indeed, the control over pinning centres can be crucial to develop superconducting devices with high critical currents [67] and for fluxonic applications [68] [69].
Finally we observed a non-negligible effect of oscillating magnetic fields on the entrance and expulsion of single vortices. Further measurements and an accurate theoretical description will be able to give a satisfactory explanation of this effect. Moreover, additional data may improve the understanding of the role of magnetic field in the onset of surface barriers, and give new insights into the process of single-vortex nucleation.

STM thus proved to be an incredibly powerful tool to observe vortex matter and to investigate its behaviour in mesoscopic systems. Future improvements can be proposed in different directions to tackle numerous questions. Increasing the confinement regime and improving the quality of the samples are necessary steps in order to investigate different predicted phenomena in superconducting nanostructures, such as symmetry-induced vortex-antivortex pairs, which have not been experimentally observed yet. Vortex motion in nanostructures can also be explored using lock-in techniques, as already done on plain films [70]. Implementing also hybrid AFM-STM techniques can expand the range of topics to investigate, such as combined structures of superconducting and insulating materials.
A deep understanding of vortex behaviour in superconductors is of key relevance to solve many of the current problems regarding the design of novel devices such as single-photon superconducting detectors, superconducting transport lines and superconducting magnets. On a more general level, vortices in superconductors can also be used as toy-systems that

mimic others, such as colloidal particles, bacteria or even artificial spin containers for quantum annealing investigation, proving that vortex matter is a highly versatile sector for applications while keeping room for fundamental research. In this framework, the ability of STM to directly probe the local density of states with atomic resolution unfolds a plethora of future possibilities to investigate, not only in superconductors, numerous quantum effects that haven't been completely understood so far.

Acknowledgements

This master thesis has been mostly carried out during my Erasmus experience in Leuven. In these six months I had the chance to meet so many people that helped me in different ways that it's for sure hard to remember all of them.
My first thanks goes to my supervisors: Prof. Joris Van de Vondel and Prof. Giovanni Mattei, who gave me the opportunity to work in the Nanoscale Superconductivity and Magnetism group at the KU Leuven and provided a constant support throughout the whole duration of this work.
I owe a special thanks to Lise and Matias: not only for your daily help and teachings, but also for stimulating discussions that gave me an insight into the world of research and cleared my mind about my future.
Thanks also to Jeroen, Cun and Vyacheslav for some good company in the office during the writing part of the thesis.
A big thanks goes to all the people I had the luck to meet in Leuven, with whom I shared most of the best moments of my Erasmus. I will not forget these 6 months with all of you guys, and I'm sure there will be time for a reunion one day.
I would like to thank my family, for giving me the best support I could have asked for and always encouraging me to choose my own path.
My last thanks goes to all of my friends, without whom I would have never achieved all of this. No matter how far we may end up being, there will always be time to be together again.

Bibliography

[1] Schmidt V. V., *The Physics of Superconductors - Introduction to Fundamentals and Applications*, Springer Berlin Heidelberg, (1997).

[2] Rossi L., *Manufacturing and Testing of Accelerator Superconducting Magnets*, arXiv:1501.07164, (2015).

[3] Cooper L., *Bound Electron Pairs in a Degenerate Fermi Gas*, Phys. Rev., **104**, 1189, (1956).

[4] Moschalkov V. V. and Fritzsche J., *Nanostructured Superconductors*, World Scientific Publishing, (2011).

[5] Johnson M. W. et al., *Quantum annealing with manufactured spins*, Nature **473** 194-198 (2011).

[6] Onnes H.K., *The resistance of pure mercury at helium temperatures*, Commun. Phys. Lab. Univ. Leiden **12**:120 (1911).

[7] Meissner W. and Ochsenfeld R., *Ein neuer effekt bei Eintritt der Supraleitfahigkeit*, Naturwissenschaften **21** (44): 787–788, (1933).

[8] V. L. Ginzburg and L. D. Landau, Zh. Eksp. Teor. Fiz., **20** 1064 (1950).

[9] *Press Release: The Nobel Prize in Physics 2003*, Nobelprize.org, Nobel Media AB 2014.

[10] Bardeen J. et al, *Microscopic Theory of Superconductivity*, Phys. Rev. **106**, 1, pp. 162-164.

[11] Landau L. D. and Lifshitz E. M., *Statistical Physics*, Nauka, Moscow, 3rd edition, (1976).

[12] de Gennes P. G., *Superconductivity of metals and alloys*, Benjamin New York (1966).

[13] A. A. Abrikosov, Zh. Eksp. Theor. Teor. Fiz. **32** 1442 (1957).

[14] Essmann U. and Trauble H., *The Direct Observation of Individual Flux Lines in Type II Superconductors*, Phys. Lett. A **24** 526, (1967).

[15] Geim A. K. et al., *Phase transitions in individual sub-micrometre superconductors*, Nature **390** 259 (1997).

[16] Nishio et al., *Scanning Hall probe microscopy of vortex patterns in a superconducting microsquare*, Phys. Rev. B., **77** 012502 (2008).

[17] Kokubo N. et al., *Scanning SQUID microscope study of vortex polygons and shells in weak pinning disks of an amorphous superconducting film*, Phys. Rev. B **82**, 014501 (2010).

[18] Bardeen J. and Stephen M. J., *Theory of the Motion of Vortices in Superconductors*, Phys. Rev. **140** 1197-1207 (1965).

[19] Baelus B. J. and Peeters F. M., *Dependence of the Vortex Configuration on the Geometry of Mesoscopic Flat Samples*, Phys. Rev. B **65**, 104515 (2002).

[20] Buzdin A. I. and Brison J.P., *Vortex structures in small superconducting disks*, Phys. Lett. A **196**, 267 (1994).

[21] Zhao H. J. et al., *Vortex States in Mesoscopic Supercondutig Squares: Formation of vortex shells*, Phys. Rev. B **78**, 104517 (2008).

[22] Chibotaru L.F. et al., *Ginzburg-Landau description of confinement and quantization effects in mesoscopic superconductors*, J. Math. Phys. **46**, 9, p. 095108

[23] Schweigert V. A. et al., *Vortex Phase Diagram for Mesoscopic Superconducting Disks*, Phys. ev. Lett. **81**, 2783 (1998).

[24] Chibotaru et al., *Symmetry-induced formation of antivortices in mesoscopic superconductors*, Nature **408** pp. 833-835.

[25] Moschchalkov V. V. et al., *Effect of sample topology on the critical fields of mesoscopic superconductors*, Nature **373** 319-322 (1995).

[26] Cren T. et al., *Vortex Fusion and Giant Vortex States in Confined Superconducting Condensates*, Phys. Rev. Lett. **107**, 097202 (2011).

[27] Roditchev et al., *Direct observation of Josephson vortex cores*, Nature Physics **11** 332-337 (2015).

[28] de Broglie L., Comptes rendus, Vol. 177, 1923, pp. 507-510.

[29] Nimtz G. and Haibel A., *Zero Time Space*, 2008, Wiley-VCH.

[30] Gamow G., Z. Phys. **51** 204.

[31] Gurney R. W. and Condon E. U., *Quantum Mechanics and Radioactive Disintegration*, Nature **122**, 439.

[32] Esaki L., *New Phenomenon in Narrow Germanium p-n Junctions* Phys. Rev. **109**, 603.

[33] *Press Release: The Nobel Prize in Physics 1973*, Nobelprize.org, Nobel Media AB 2014.

[34] Bardeen J., *Tunneling from a Many-Particle Point of View*, Phys. Rev. Lett. **6**, 2 (1961)

[35] Buchner F., *STM Investigation of Molecular Architecture of Porphyrinoids on a Ag(111) Surface*, Springer-Verlag Berlin Heidelberg (2010).

[36] Wiesendanger R., *Scanning Probe Microscopy and Spectroscopy, Methods and Applications*, Cambridge University Press, (1994).

[37] Giaever I., *Energy Gap in Superconductors Measured by Electron Tunneling*, Phys. Rev. Lett. **5**, 4 (1960).

[38] Serrier-Garcia L., *Vortex confinés dans des nanostructures de Pb/Si(111) étudiés par microscopie à effet tunnel*, PhD Thesis (2014).

[39] Bezryadin A., *Superconductivity in Nanowires. Fabrication and Quantum Transport*, Wiley-VCH Verlag GmbH & Co. KGaA (2013).

[40] Graybeal J. M. and Beasley M. R., *Localization and interaction effects in ultrathin amorphous superconducting films*, Phys. Rev. B **29** 4167 (1984).

[41] Nečas et al., *Gwyddion: an open-source software for SPM data analysis*, Cent. Eur. J. Phys. **10**(1) 181-188 (2012).

[42] Farrell I. L., *Growth of Metal-Nitride Thin Films by Pulsed Lasr Deposition*, PhD Thesis (2010).

[43] Willmott P. R. and Huber J. R., *Pulsed laser vaporization and deposition*, Rev. Mod. Phys. **72** pp. 315-328 (2000).

[44] Deutscher G. and de Gennes P. G. in *Superconductivity*, edited by Parks R. D., Marcel Dekker, New York (1969).

[45] Tashiro H. et al., *Unusual thickness dependence of the superconducting transition of α-MoGe thin films*, Phys. Rev. B **78**, 014509 (2008).

[46] Binnig G. et al, *Atomic Force Microscope*, Phys. Rev. Lett. **56** 930-933 (1986).

[47] Stirling J., https://commons.wikimedia.org/wiki/File:AFM_Amplitude_Modulation.svg/ /media/File:AFM_Amplitude_Modulation.svg.

[48] Binnig J. and Rohrer H., *Scanning Tunneling Microscopy*, Surface Science **126** 236-244 (1983).

[49] *Press Release: The Nobel Prize in Physics 1986*, Nobelprize.org, Nobel Media AB 2014.

[50] Woestke S., PhD Thesis, Inst. f. Exp. u. Ang. Phys. der CAU Kiel (2002).

[51] www.parkafm.com .

[52] Cren T. et al., *Ultimate Vortex Confinement Studied by Scanning Tunneling Microscopy*, Phys. Rev. Lett. **102** 127005 (2009).

[53] Peeters F. M. et al., *Vortex states in mesoscopic superconductors*, Physica E **18** 312-315 (2003).

[54] Baelus B. J. et al., *Influence of surface defects on vortex penetration and expulsion in mesoscopic superconductors*, Phys. Rev B **71** 024514 (2005).

[55] Baelus B. J. et al., *Multivortex and giant vortex states near the expulsion and penetration fields in thin mesoscopic superconducting squares*, Phys. Rev. B **73**, 024514 (2006).

[56] Schweigert V. A. and Peeters F. M., *Flux Penetration and Expulsion in Thin Superconducting Disks*, Phys. Rev. B **83** 12 (1999).

[57] Fink H. J. and Presson A. G., *Stability Limit of the Superheated Meissner State due to Three-Dimensional Fluctuations of the Order Parameter and Vector Potential*, Phys. rev. **182** 498 (1969).

[58] Schweigert V. A. and Peeters F. M., *Influence of the confinement geometry on surface superconductivity*, Phys. Rev. B **60** 3084 (1999).

[59] Poole C. P. Jr et al., *Superconductivity*, Elsevier Ltd. (1995).

[60] Gutierrez J., *First vortex entry into a perpendicular magnetized superconducting thin film*, Phys. Rev. B **88** 184504 (2013).

[61] Lin F. P.-J. and Gurevich A., *Effect of impurities on the superheating field of type-II superconductors*, Phys. Rev. B **85** 054513 (2012)

[62] Kramer L., *Stability limits of the Meissner state and the mechanism of spontaneous vortex nucleation in superconductors*, Phys. Rev. **170** pp. 475-480 (1968).

[63] Bean C. P. and Livingston J. D., *Surface Barrier in Type-II Superconductors*, Phys. Rev. Lett. **12** 14 (1964).

[64] Civale et al., *Vortex Confinement by Columnar Defects in $YBa_2Cu_3O_7$ Crystals: Enhanced Pinning at High Fields and Temperatures* Phys. Rev. Lett. **67** 1164 (1990).

[65] Ge J.-Y. et al., *Bound vortex dipoles generated at pinning centres by Meissner current*, Nature Communications **6** 6573 (2015)

[66] Van Bael M. J., *Regular arrays of magnetic dots and their flux pinning properties*, PhD Thesis (1998).

[67] Bugoslavsky T. et al., *Enhancement of the high-magnetic-field critical current density of superconducting MgB2 by proton irradiation*, Nature **411** 561-563 (2001).

[68] Linke H. et al., *Experimental Tunneling Ratchets*, Science **286** pp. 2314-2317 (1999).

[69] Villegas J. E. et al., *A Superconducting Reversible Rectifier That Controls the Motion of Magnetic Flux Quanta*, Science **302** pp. 1188-1191 (2003).

[70] Timmermans et al., *Dynamic Visualization of Nanoscale Vortex Orbits*, ACS Nano **8**(3) pp 2782-2787 (2014).